



Disentangling methane and carbon dioxide sources and transport across the Russian Arctic from aircraft measurements

Clément Narbaud¹, Jean-Daniel Paris^{1,2}, Sophie Wittig¹, Antoine Berchet¹, Marielle Saunois¹, Philippe Nédélec³, Boris D. Belan⁴, Mikhail Y. Arshinov⁴, Sergei B. Belan⁴, Denis Davydov⁴, Alexander Fofonov⁴, Artem Kozlov⁴

¹ Laboratoire des Sciences du Climat et de l'Environnement, IPSL, Orme des Merisiers, CEA-CNRS-UVSQ, 91190 Gif-sur-Yvette, France

² Climate and Atmosphere Research Centre (CARE-C), The Cyprus Institute, Nicosia, 2121, Cyprus

³ LAERO, Université de Toulouse, UT3, CNRS, IRD, Toulouse, France

⁴ Independent researcher

Correspondence to: Jean-Daniel Paris (jean-daniel.paris@lscce.ipsl.fr)

Abstract. A more accurate characterization of the sources and sinks of methane (CH₄) and carbon dioxide (CO₂) in the vulnerable Arctic environment is required to better predict climate change. A large-scale aircraft campaign took place in September 2020 focusing on the Siberian Arctic coast. CH₄ and CO₂ were measured in situ during the campaign and form the core of this study. Measured ozone (O₃) and carbon monoxide (CO) are used here as tracers. Median CH₄ mixing ratios are fairly higher than the monthly mean hemispheric reference (Mauna Loa, Hawaii, US) with 1890-1969 ppb vs 1887 ppb respectively, while CO₂ mixing ratios from all flights are lower (408.09-411.50 ppm vs 411.52 ppm). We also report on three case studies. Our analysis suggests that during the campaign the European part of Russia's Arctic and Western Siberia were subject to long-range transport of polluted air masses, while the East was mainly under the influence of local emissions of greenhouse gases. The relative contributions of the main anthropogenic and natural sources of CH₄ are simulated using the Lagrangian model FLEXPART in order to identify dominant sources in the boundary layer and in the free troposphere. In western terrestrial flights, air masses composition is influenced by emissions from wetlands and anthropogenic activities (waste management, fossil fuel industry and to a lesser extent the agricultural sector), while in the East, emissions are dominated by freshwaters, wetlands, and the oceans, with a likely contribution from anthropogenic sources related to fossil fuels. Our results highlight the importance of the contributions from freshwater and oceans emissions. Considering the large uncertainties associated to them, our study suggests that the emissions from these aquatic sources should receive more attention in Siberia.

1 Introduction

The increasing greenhouse gas burden in the atmosphere led to a global surface temperature rise of 1.09 °C in the last decade (2011-2020) compared to the last decades of the 19th century (1850-1900) (Masson-Delmotte et al., 2021). The global mean mixing ratio of carbon dioxide (CO₂) reached 413.2±0.20 ppm in 2020 (WMO, 2021). Anthropogenic CO₂ sources are dominated by fossil fuel combustion and cement production (9.6±0.5 GtC yr⁻¹) and land-use change (1.6±0.7 GtC yr⁻¹). While



35 these emissions are steadily increasing, the main sinks of CO₂, terrestrial vegetation (3.4±0.9 GtC yr⁻¹) and oceans (2.5±0.6 GtC yr⁻¹) have taken up a rather stable proportion (about 56% per year) of emissions from human activities albeit with regional differences (Friedlingstein et al., 2020; Masson-Delmotte et al., 2021).

Methane (CH₄), the second most abundant anthropogenic greenhouse gas, reached 1889±2 ppb in the atmosphere in 2020 (WMO, 2021), but has a global warming potential about 32 times higher than CO₂ on a 100-year horizon (Etminan et al., 2016). Since 2007, the CH₄ mixing ratio has been constantly increasing, up to 8-9 ppb yr⁻¹ corresponding to an increase of the atmospheric burden of about 25 Tg CH₄ yr⁻¹ (Platt et al., 2018). A total of 576 Tg CH₄ yr⁻¹ has been injected into the atmosphere during the 2008-2017 decade combining anthropogenic and natural sources (Saunio et al., 2020). Anthropogenic emissions represent 60% of global total methane emissions with agriculture and waste management (178 to 206 Tg CH₄ yr⁻¹) and fossil fuels exploitation (178 to 206 Tg CH₄ yr⁻¹). On a global scale, wetlands are the largest natural methane emission source (153 to 227 Tg CH₄ yr⁻¹) (Kirschke et al., 2013; Lan et al., 2021). Emissions from freshwaters have estimates ranging widely between 60 and 180 Tg CH₄ yr⁻¹ (Saunio et al., 2016) and are mainly driven by diffusion, ebullition and release from bubble storage (Matthews et al., 2020). Fluxes from aquatic sources may be underestimated (Rosentreter et al., 2021). Ocean emissions by diffusion and ebullition are estimated to range between 2 and 40 Tg CH₄ yr⁻¹. However, these estimated CH₄ emissions could potentially be higher due to large gas hydrate reservoirs on the seabed of Arctic Ocean (Platt et al., 2018). Widely debated emissions attributed to marine sources including methane hydrates dissociation have already been observed in the region (Shakhova et al., 2010; Berchet et al., 2016; Platt et al., 2018; Berchet et al., 2020; Thornton et al., 2020; Steinbach et al., 2021).

Siberia and the Russian Arctic are significant contributors to the CH₄ budget. Half of Siberian emissions originate from fossil fuel exploitation (about 17 Tg CH₄ yr⁻¹), one third from natural wetlands (about 13 Tg CH₄ yr⁻¹) and a minor contribution from agriculture and waste (about 5 Tg CH₄ yr⁻¹) for a total average of 38 Tg CH₄ yr⁻¹ (Saunio et al., 2016). The multiplicity of the sources and the seasonality of emissions (Berchet et al., 2015; Belikov et al., 2019) influence CH₄ variability over Siberia. Many uncertainties in the CH₄ emissions in Siberia therefore remain (Berchet et al., 2016; Elder et al., 2020; Matthews et al., 2020; Wik et al., 2016; Thornton et al., 2016). Uncertainties are driven by the multitude of adjacent sources present in the region: natural wetlands, freshwaters (lakes, ponds and streams), oceans and anthropogenic activities (leaks from increasing oil and gas extraction and transport, as well as regional agriculture and waste management) and biomass burning. In addition to the currently dominant sources, the thawing of continental and submarine permafrost could release massive amount of carbon in the atmosphere since Siberia is considered to be one of the world's largest terrestrial carbon reservoirs (Belikov et al. 2019). Soils in the permafrost region retain twice as much carbon as the atmosphere does (Turetsky et al., 2019).

To reduce uncertainties at the scale of Siberia, atmospheric measurements have been performed at tower observatories (Belikov et al., 2019; Sasakawa et al., 2010; Sasakawa et al., 2017; Fujita et al., 2020), during oceanographic campaigns (Thornton et al., 2016; Berchet et al., 2020; Steinbach et al., 2021) or even by train (Skorokhod et al., 2016). The YAK-AEROSIB project organizes intensive campaigns since 2006 across all of Siberia (Paris et al., 2008; Paris et al., 2010). These annual campaigns



provide measurements of atmospheric concentrations of CO₂, CH₄, O₃, and carbon monoxide (CO) and aerosols with an objective to better understand regional sources, dynamical processes and long-range transport in Siberia (Paris et al., 2008; Berchet et al., 2013). In situ measurements have the potential to document carbon sources and sinks in Siberia, and therefore to ultimately establish a more accurate estimations of future greenhouse gas trajectories. The previous campaigns have highlighted several key mechanisms in this poorly-studied region by representing vertical profiles of several greenhouse gases to determine the origin and impact of polluted air masses (Paris et al., 2008), identifying the source of upper tropospheric O₃ depletion (Berchet et al., 2013) or also bringing new insights on specific events like the extensive wildfires that occur in Siberia during summer (Paris et al., 2009; Antokhin et al., 2018). In the present work, we analyze data from the last YAK-AEROSIB campaign that took place during September 2020 with a specific focus on Northern Russia and the coastal Arctic Ocean. This campaign included 13 flights across Russia with dedicated flights over the northern seas of Barents, Kara and Laptev, and the very East of the region with Bering Strait, the East Siberian Sea and the Chukchi Sea.

The present study focuses on the distribution of CH₄ and CO₂. This paper aims more specifically to identify and quantify the respective contributions from regional sources of CH₄ during the first half of September 2020 in the Russian Arctic. We document the measurement and data collected during the campaign. Ozone and carbon monoxide are used as tracers for the interpretation of CO₂ and CH₄ mixing ratio variability. Tropospheric ozone is a harmful pollutant produced from precursors including CO and CH₄ (Saunois et al., 2016), while CO is a pollutant and a minor greenhouse gas produced by combustion processes.

In Sect. 2, we first describe the study area and the in-situ instrumentation for continuous measurements of CO₂, CH₄, O₃, and CO. We also explain our approach and the inputs to determine the contributions of each CH₄ source to the measurements made during the campaign, which is mainly achieved by combining the Lagrangian FLEXible TRAjectory model (FLEXPART) of transport and diffusion, with methane flux inventories. In Sect. 3 we present the 47 vertical profiles taken during the campaign with an emphasis on CO₂ and CH₄ mixing ratios. We then describe three case studies based on specific signatures in species variability. We also discuss how this data coincides with simulations of CH₄ enhancements linked to anthropogenic and natural sources to give insights on the main CH₄ contributions at the time of the flight. We conclude by discussing the respective importance of anthropogenic activities and aquatic sources on CH₄ variability over Western Russia and Northeastern Siberia.

2 Methods

2.1 Description and synoptic situation of the campaign

The flight route of the September 2020 campaign is shown in Fig. 1 and the campaign is described in Table 1. An overview of the campaign can be found in Belan et al. (2022). The aircraft used for the campaign was the “Optik” Tupolev-134A-3M (SKh) operated by the V.E. Zuev Institute of Atmospheric Optics (Tomsk, Russia) (Anokhin et al., 2011). The maximum range of



the plane is 3000 km with an average observed airspeed of 172 m s^{-1} and a vertical speed of 6.5 m s^{-1} for both ascents and descents. The plane configuration is illustrated in Fig. 2 and more details can be found in Antokhin et al. (2011).

The campaign took place between September 4th and 17th, 2020. Thirteen different flights covered Russia from 55° N to 76° N between 40° E and 172° W for a cumulative ground distance of 25000 km with altitudes up to 11 km. The flights are grouped in two different categories: 1) loops above lands and oceans to explore specific environments with flight legs at typical altitudes of 200, 500 and 5000 m (these flights are referred to with a prefix “L”), and 2) transit flights between airports (prefix “T”).

The campaign started in Novosibirsk and ended in Bogashevo (Tomsk airport). The first flights (T1, L1, T2, L2 and T3) crossed the cities of Arkhangelsk and Naryan-Mar and encompassed different biomes such as taiga (boreal forest), extensive wetlands and steppe regions (Belikov et al., 2019). Then the plane travelled along the Northern shores of the Russian Federation (T4, L3 and T5), above section of the Arctic Ocean in the seas of Kara, Laptev and the East Siberian Sea, crossing the small towns of Sabetta and Tiksi. The Arctic Ocean is at its lowest annual sea-ice extent in September and September 2020 was the second record low in Arctic sea-ice extent after 2012 (Fetterer et al., 2017). The seas that were covered by the campaign were essentially free of ice during the campaign (Fig. B1). The East Siberian Arctic Shelf (ESAS) contains up to 40% of Arctic marine permafrost (Ruppel, 2015). Several loops (L4.1, L4.2, and L4.3) were carried out in the Russian Far East characterized by Arctic deserts, tundra, and forest tundra for the northern regions while the south is dominated by forests (Petäjä et al., 2021). All these loops used the airport of Ugolny (Anadyr). The final transit flights (T6 and T7) crossed regions covered by forests of coniferous trees and by agricultural lands to the South (Bartalev et al., 2003), and landed at the airports of Yakutsk and Tomsk respectively. Large oil and gas (O&G) infrastructures (Yakutsk pipeline, Kenai terminal in Alaska) and coal mines (Ammam, Vorgashorskaya) from the Global Monitor Energy (2022) database are displayed on the map.

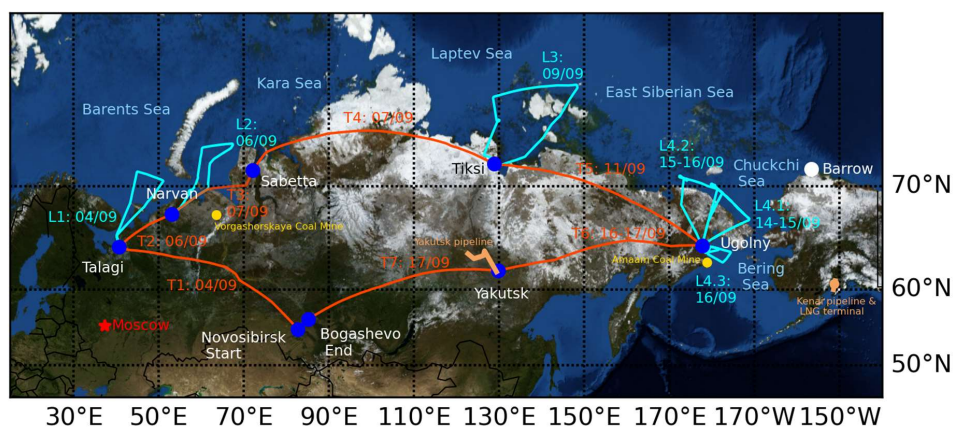


Figure 1: September 2020 campaign flight plan. The 13 flights are indicated either as “loop” (prefix L, cyan line) or “transit” (prefix T, orange line). Oil and gas (O&G) infrastructures and coal mines are shown in light orange and yellow respectively (data



from “Global Coal Mine Tracker” and “Global Fossil Infrastructure Tracker”, Global Energy Monitor 2022, under CC BY-NC-SA 4.0 License). Map background: “Blue Marble Next Generation”, September 2004 (Stöckli et al., n.d.).

Table 1: Campaign description

Flight	Date UTC	Time UTC	Local Time	Airports	Latitude	Longitude
T1	04 Sept. 20	06:55-11:01	13:55-15:01	Novosibirsk North-Talagi	55-65° N	83-41° E
L1	04 Sept. 20	12:58-17:06	15:58-20:06	Talagi	65° N	41° E
T2	06 Sept. 20	08:07-09:31	11:07-12:31	Talagi-Naryan Mar	65-68° N	41-53° E
L2	06 Sept. 20	10:55-14:36	13:55-17:36	Naryan Mar	68° N	53° E
T3	07 Sept. 20	05:01-06:27	08:01-11:27	Naryan Mar-Sabetta	68-71° N	53-72° E
T4	07 Sept. 20	08:14-10:48	11:14-19:48	Sabetta-Tiksi	71-72° N	72-129° E
L3	09 Sept. 20	03:09-06:57	12:09-15:57	Tiksi	72° N	129° E
T5	11 Sept. 20	01:48-05:00	10:48-17:00	Tiksi-Ugolny	72-65° N	129-178° E
L4.1	14-15 Sept. 20	23:28-02:57	11:28-14:57	Ugolny	65° N	178° E
L4.2	15-16 Sept. 20	22:32-01:42	10:32-13:42	Ugolny	65° N	178° E
L4.3	16 Sept. 20	03:38-05:51	15:38-17:51	Ugolny	65° N	178° E
T6	16-17 Sept. 20	23:16-02:39	11:16-11:39	Ugolny-Yakutsk	65-62° N	178-130° E
T7	17 Sept. 20	03:57-07:49	14:57-14:49	Yakutsk	62° N	130° E

125

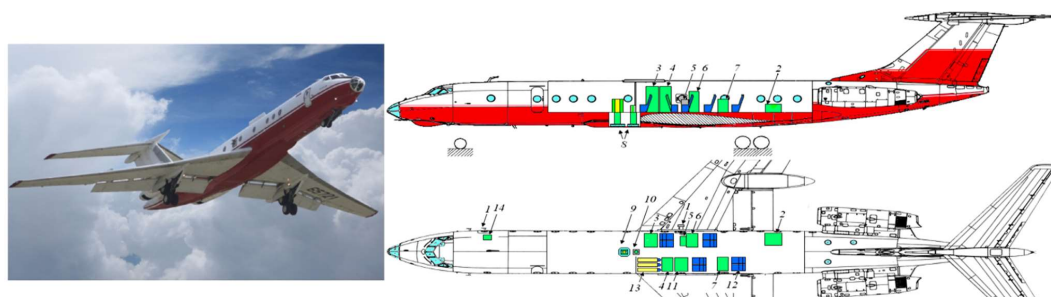


Figure 2: Arrangement of the instrument suite on board of the OPTIK TU-134 aircraft laboratory: 1 – ambient air inlets and RH&T probe; 2 – aircraft electrical power distribution unit (28 VDC); 3, 4, 5, 6 – inverters (28 VDC/220 VAC) and UPSs (Delta RT-2K); 7 – aerosol instrument rack: aethalometer (MDA-02) and photoelectric aerosol nephelometer (FAN-M); 8 – aerosol instrument rack: diffusional particle sizer (DPS), optical particle counter (Grimm 1.109), filter and bioaerosol sampling suite; 9 – navigation system (CompaNav-5.2 IAO); 10 – gas analysis rack: CO₂/CH₄/H₂O (Picarro G2301-m); 11 – gas analysis rack: O₃ (TEI Model 49C), CO (TEI Model 48C); 12 – spectroradiometer (Spectral Evolution PSR-1100F); 13, 14 – aerosol lidars; 15 – camera hatches; 16 – ambient air inlet; 17 – sampling unit for organic aerosol analysis; 18 – gas analysis rack: NO_x (Thermo

130



135 Scientific Model 42i-TL); 19 – main data acquisition system (NI PXI-1042); 20 – GLONASS/GPS antennas. Copyright to Mikhail Yu. Arshinov

140 Figure 3 shows the geopotential height at 500 hPa as provided in the dataset ERA5 from the European Centre for Medium-Range Weather Forecasts; (ECMWF; Hersbach, 2018) on the 6th and the 16th of September. At the beginning of the campaign (Fig. 3a), there was a low-pressure system over central Siberia (80° E, 60° N) and a ridge coming from Western Europe and going in a north-easterly direction to the seas of Barents and Kara. The period was characterized by an “Omega” whirling around troughs over Eastern Europe and eastern Asia that can be seen distinctly at the end of the campaign (Fig. 3b). The combination of these two events lifted an air mass most likely affected by western European emissions into the free troposphere over Siberia during the campaign. This may have influenced greenhouse gases concentrations as measured during the campaign. Over Eastern Siberia (180° E, 55° N), there was a low-pressure system and winds blown from western Alaska to
145 Bering Strait (Fig. 3b).

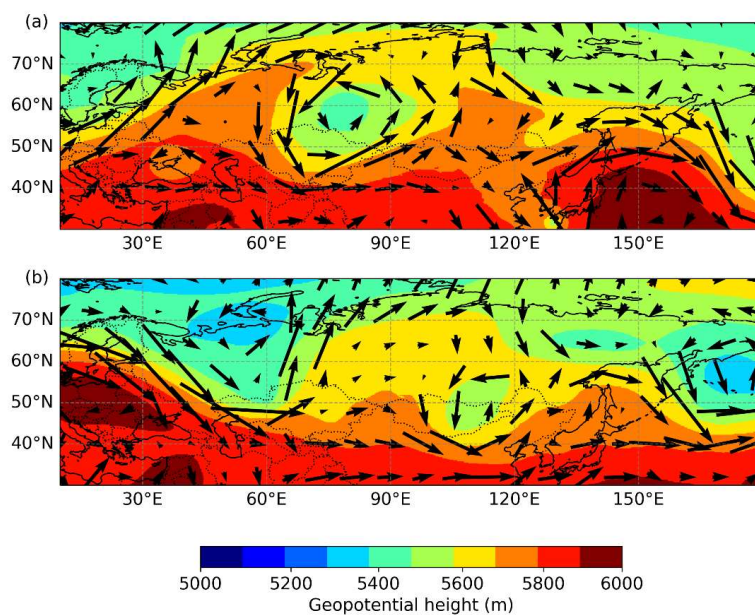


Figure 3: (a) Geopotential height and wind (speed and direction) at 500 hPa from ECMWF reanalyses for 06 September at 13:00 UTC. (b) Same as (a) for 15 September at 01:00 UTC

150 A series of 47 vertical profiles was collected, each lasting between 20 and 30 min. Loop flights were composed of three ascending and descending profiles. Transit flights had only vertical profiles during take-off and landing, and took place at high



altitude (about 10 km) in between. The plane stayed at horizontal plateaus when top altitudes were reached between 9000 m and 11000 m, as well as close to the ground at about 200 m and some on descents at 5000 m and at 500 m. 60% of the measurements were taken above the Arctic Circle ($> 66^\circ$ N). About 80% of the data was acquired above 2000 m which is generally above the planet boundary layer (BL) at these latitudes and time of the year.

2.2 Instrumentation of the campaign

For in situ analysis air is sampled from inlets. The length of the tubes between the inlets and instruments was 3 m. Concentrations of CO_2 and CH_4 were measured by a Picarro G2301-m GHG analyzer using Cavity Ring-Down Spectroscopy. It is a modification of the G2301 model specially conceived for aircraft measurements which is designed to minimize effects induced by aircraft vibration and roll, and suitable for rapidly changing altitude (up to 1000 m min^{-1}) and temperature (up to $15^\circ \text{C hr}^{-1}$) conditions. It has an acquisition rate of 1 Hz and a precision of <0.20 ppm for CO_2 and <1.5 ppb for CH_4 . Water vapor mole fraction is also quantified to include internal water dilution correction and thereby express dry air mole fractions of carbon dioxide and methane. Three calibration gases are transported in high-pressure cylinders with respective CO_2 mixing ratios of 370.91 ± 0.005 ppm, 390.33 ± 0.009 ppm and 430.30 ± 0.006 and CH_4 mixing ratios of 1814.35 ± 0.150 ppb, 1960.99 ± 0.094 ppb, and 2205.01 ± 0.106 ppb. Their values were determined before the campaign at Laboratoire des Sciences du Climat et de l'Environnement (LSCE) according to World Meteorological Organization (WMO) standards (Paris et al., 2008). The drift is then corrected according to the difference between the measurements and the calibrated value of the reference gas. The whole campaign has been sampled at an interval of 1 s without data gaps, except for the transit T1 (the first of the series) during which the instrument software “froze” for the first half of the flight and it was restarted.

The calibrated measurements can be compared to values of reference of stations at Mauna Loa, Hawaii (19.54° N, 155.58° W, 3397 m a.s.l) (Oltmans and Levy 1994; Dlugokencky et al., 2021a; Dlugokencky et al., 2021b) and Mace Head, Ireland (53.20° N, 09.54° W, 25 m a.s.l) (Hazan et al., 2016) that can be considered as background sites for CO_2 , CH_4 , CO (only Mace Head) and O_3 (only Mauna Loa) concentrations during September 2020. Measurements from Barrow, Alaska (71.32° N, 156° W, 11 m a.s.l, see Fig. 1) were also used for comparison.

Ozone was measured by a commercial fast response ozone analyzer (Thermo Environmental Instruments Model 49C USA), with modifications for internal calibration and aircraft operation safety. It is based on UV absorption in two parallel cells and has a precision of 2 ppb for an integration time of 4 s. In practice, values have been acquired with periods that vary between 4 and 10 s. Air is pressurized prior to the detection by a Teflon KNF Neuberger pump model N735 also used for CO. Before the campaign, the instrument has been calibrated against a NIST related reference calibrator Model49PS and verification of the O_3 analyzer have been made before and after the campaign. The length of the Teflon tubes between the inlet and O_3 and CO analyzers was 2m.

Carbon monoxide is acquired by an instrument based on a commercial infrared absorption correlation gas analyzer (Thermo Electron Model 48C, USA). It has been improved with addition of a periodical in-flight accurate zero measurements, new IR



185 detector, pressure increase and regulation in the absorption cell, increased flow rate to 4 l min⁻¹, water vapor trap and ozone
filter. The response time of the instrument is 30 s and it has a precision of 5 ppb, with a lower detection limit at 10 ppb (“YAK-
Aerosib Measurements”, 2021). For this campaign, the CO data were not post-processed due to technical problems and were
therefore of lower quality than in previous studies. We applied a median filter with a kernel size of 75 samples, CO standard
deviations were ranging between 10 and 35 ppb for mean mole fractions between 73 and 103 ppb. We decided to not use CO
measurements for a quantitative study but as a tracer for analysis of the other gases.

190 **2.3 Back trajectories with the Lagrangian model FLEXPART**

We used the Lagrangian particle transport and dispersion model FLEXPART (Stohl et al., 1998; Stohl and Thomson 1999;
Stohl et al., 2005; Pisso et al., 2019) for long-range transport analysis and for determining the origin of the polluted air masses
measured during the campaign. We adopted the backward (“receptor-oriented”) approach of the model suitable when the
number of sources is superior to the number of receptors and designed to quantify the remote contributions in a single plume
195 (Seibert and Frank 2004). In our configuration FLEXPART computes the position of 2000 particles backwards in time,
following the atmospheric conditions with a stochastic contribution representing the diffusion (including small scale turbulence
not included in averaged meteorological fields) (Fleming, Monks, and Manning 2012). These implementations allow a more
realistic representation of transport in planet boundary layer. The lifespan of the virtual particles was set to 10 d as the transport
precision decreases after 10 days due to accumulated transport errors and insufficient number of particles to represent it (Stohl
200 et al., 1995). The meteorological inputs were ERA5 datasets from ECMWF with a spatial resolution of 1° and a temporal
resolution of 3 h covering the north hemisphere, limiting the resolution of the output grid to 0.5° x 0.5°. A simulation was
performed for each flight, beginning 10 days before the first acquisition and ending with the last acquisition. Receptor (i.e.
aircraft) positions every 1 s during the campaign are aggregated in four dimensions boxes (0.1° x 0.1° x 100 m x 60 s). The
potential emission sensitivity (PES) calculated by the model for each receptor position is defined as the residence time of the
205 backward particles in a grid cell below a threshold altitude (here 500 m and 2000 m). We convolved this output with CH₄ flux
inventories to get maps of potential sources contributions that are integrated over the Northern Hemisphere to finally get the
simulated mixing ratios of each source every minute. To be compared with simulations, the measured mole fractions were
down-sampled into 1-minute bins and the values were averaged. In addition, the background defined as the minimal mole
fraction for each flight was removed from each value to have comparable CH₄ enhancements.

210 **2.4 Methane flux inventories**

For the present study, five categories of CH₄ sources were considered. Emissions of CH₄ by anthropogenic activities were
characterized with EDGAR v6.0 (Emission Database for Global Atmospheric Research from PBL Netherlands Environmental
Assessment Agency) with a grid resolution of 0.1° x 0.1° (Crippa et al., 2019). EDGAR inventories are published as yearly or
monthly files. We chose to use the month of September 2018 (the last available) to benefit from the seasonality of the



215 emissions. We aggregated the 21 EDGAR sectors into three categories: agriculture, exploitation and use of fossil fuels and waste management (see grouping definition in Table A1).

Biomass burning and wildfires emissions were represented using GFED4.1s (Global Fire Emissions Database) based on van der Werf et al. (2017) at a resolution of $0.25^\circ \times 0.25^\circ$ for the monthly mean of September 2020.

220 Wetlands fluxes were based on the process-based model ORCHIDEE as described in Ringeval et al. (2012) at a horizontal resolution of $0.5 \times 0.5^\circ$ for September 2017 only for the North Hemisphere provided to Global Carbon Project 2019 (Melton et al., 2013; Wania et al., 2013; Zhang et al., 2021).

The representation of freshwaters CH_4 fluxes, based on the work of Thonat et al. (2017), combined two inventories: the lake biogeochemical model (Blake4me) (Tan et al., 2015) for sources above 60°N and Global Lakes and Wetlands Database (GLWD3) distribution for the rest of the Northern Hemisphere (Lehner and Döll, 2004), with a resolution of $0.25^\circ \times 0.25^\circ$
225 based on data from 1971 to 2013.

The ocean fluxes were based on the work of Weber et al. (2019), a synthesis of measurements made between 1980 and 2016 with an output grid in resolution $0.25^\circ \times 0.25^\circ$ from the MarinE MethanE and NiTrous Oxide (MEMENTO) database (Kock and Bange, 2015). The total marine fluxes are provided as diffusive fluxes from sediments to the surface and ebullition of bubbles released from bottom sediments that reached the atmosphere. We combined the two fluxes in one emission map.

230 When it was possible, we preferred using inventories averaged on September instead of inventories averaged on several months to put an emphasis on the seasonality of emissions. All inventories were re-gridded to $0.5^\circ \times 0.5^\circ$ in order to be aligned with the grid of the FLEXPART footprints. Figure A1 illustrates the fluxes indexed by inventories from fossil fuel exploitation, agriculture, wetlands, freshwaters, and oceans on Northern Hemisphere.

3 Results

235 3.1 Distribution of CH_4 and CO_2 during the campaign

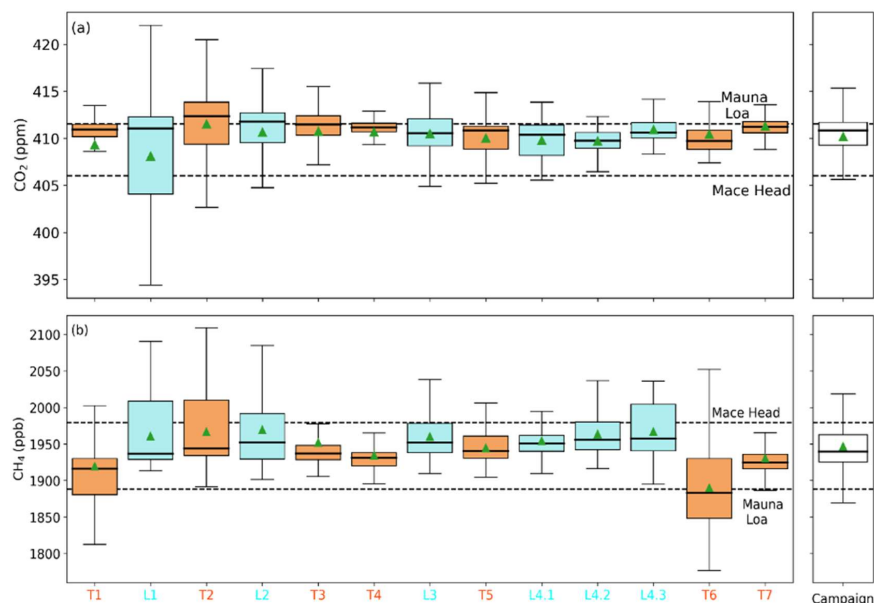
Hereafter we refer to “low altitude” and “high altitude” for data that are respectively acquired below and above an arbitrary altitude threshold of 2000 m. The majority (80 %) of the data have been measured at “high altitude”. “Low altitude” measurements are analyzed separately to highlight sensitivity to local or regional sources. Reported uncertainties are 1σ uncertainties.

240 3.1.1 CH_4 mixing ratios

The average CH_4 mixing ratio of the campaign is 1946 ± 45 ppb. This is higher than the monthly mean mixing ratio measured at Mauna Loa 1887 ppb used as Hemispheric reference. Figure 4b shows that the median value of each flight (except for T6) is above the Mauna Loa mean value. At low altitude, the average mole fraction is 2011 ± 33 ppb and so exceed both mixing ratios observed at Mauna Loa and Mace Head (1979 ppb). This suggests the possible influence of significant regional methane



245 sources. This observation is emphasized by the presence of wide interquartile ranges (especially for the first flights T1, T2, L1 and L2), pointing to strong gradients in CH₄ mole fractions (up to +200 ppb) caused by significant methane emissions close to the ground.



250 **Figure 4: (a) CO₂ mixing ratios variability by flight. Statistics for the entire campaign are shown in the right panel. The boxplot shows the interquartile range (25-75%) and the median value. The whiskers extend to the lowest and highest values, ignoring outliers beyond 1.5 times the interquartile range. Flight means are shown as green triangle. Dashed lines show respectively the mean monthly mixing ratios at Mauna Loa and Mace Head during September 2020. (b) Same as (a) for CH₄.**

Generally, loop flights exhibit a higher first quartile than transit flights for low altitude values. These specific flights have
255 indeed longer low-altitude legs and overall more frequent passages at low altitude (three for loops versus one for transits).
High CH₄ concentrations in narrow enhancements close to the seas might illustrate the contribution of regional marine and coastal sources. This will be further discussed in Sect. 3.3.

3.1.2 CO₂ mixing ratios

The average CO₂ mixing ratio of the campaign is 410.17±3.29 ppm, slightly below the seasonal average at Mauna Loa (411.52
260 ppm) but higher than the Mace Head value (406.00 ppm). Figure 4a presents the mixing ratio statistics for each flight and the whole campaign. Almost all median values are below the Mauna Loa reference, suggesting that air masses observed during



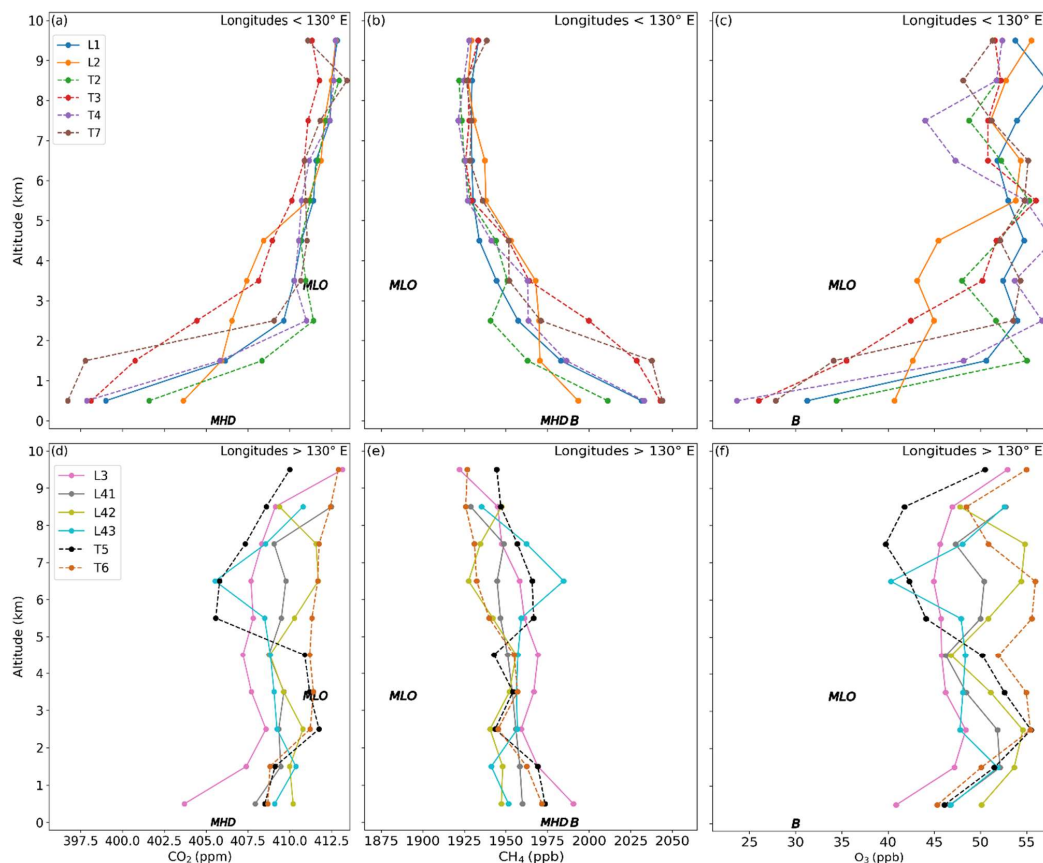
the campaign may have intersected with regional CO₂ sinks. Candidate areas potentially explaining the sink include all terrestrial biomes in Russia (Bartalev et al., 2003; Belikov et al., 2019; Petäjä et al., 2021). Flight T1 flying over the Western Siberian taiga exhibits median values at low and high altitude respectively of 397.73 ppm and 410.92 ppm (with standard
265 deviation of 4.30 ppm), highlighting the influence of these sinks.

Two flights (L1 and T2) exhibit a large variability compared to the rest. For both flights, there are considerable gradients in CO₂ mole fractions (+15 ppm and +10 ppm for respectively L1 and T2) between high and low altitudes suggesting the presence of effective sinks (forests and oceans in this case) at low altitude and the presence of “polluted” air masses at high altitude from long-range transport.

270 The highest mixing ratio measured during the campaign (451.85 ppm) was registered at the end of flight T6 while the aircraft was landing at the airport of Yakutsk. This is most likely driven by local pollution. At the time of landing the airport was fogged in (the aircraft was landed with difficulty due to the absence of enough fuel for flying to an alternate airfield).

3.2 Average vertical distribution of the gases

All data were binned every 1000 m in a range of ±500 m to get vertical profiles in Fig. 5. Data were also stratified according
275 to their longitude, separating regions West and East of the 130° E meridian. As reported in Sect. 3.1, western flights exhibit large vertical gradient in mean gas mixing ratios (high minus low altitude means ranging between -64 to -109 ppb, +9.10 to +14.80 ppm and -14 to -29 ppb respectively for CO₂, CH₄, and O₃) compared to eastern flights.



280 **Figure 5:** Flight mean vertical mixing ratio profiles for CO₂ (a, d), CH₄ (b, e), and O₃ (c, f). Top row shows flights West of 130°E while bottom row shows flights East of 130° E. Flight T1 is not shown due to missing data. Monthly mean values at Mauna Loa (MLO), Mace Head (MHD) and Barrow (B) in September 2020 are shown in each panel.

For CH₄ at low altitude, western flights (Fig. 5b) present higher mixing ratios than eastern flights (Fig. 5e) with the biggest values in T3 and T7, closely followed by L1 and T4. These high mole fractions are recorded close to Moscow, western Russian cities and Western Europe with anthropogenic emissions as well as the Vasyugan swamp (wetlands) reported as a serious CH₄ source in Belikov et al. (2019). Influence of such sources is checked in Sect. 3.4.1 using the simulated CH₄ enhancements and the footprints. On the opposite, low altitude values for eastern flights (Fig. 5e) are encompassed in a range between 1940 ppb and 1960 ppb. These mixing ratios still represent an enhancement of +60 ppb to + 80 ppb compared to the hemispheric



background (Mauna Loa monthly mean) of 1888 ppb. The references of Mace Head and Barrow respectively at 1979 ppb and
290 1991 ppb are in the same range as the easternmost flights' low altitude values but below western flights low altitude values.
For Eastern flights T5 and L4.3, a layer of elevated CH₄ mixing ratios is crossed in the mid troposphere between approximately
6 and 8 km altitude (Fig. 5c). In Flight L4.3, for example, the vertical CH₄ gradient represents an excess of ~20 ppb between
6500 m and 8500 m compared to the underlying layer (between 4500 m and 6500 m). This increase of CH₄ at top altitudes for
flight L4.3 correlates with a decrease of O₃ mole fraction of -10 ppb between 7500 m and 8500 m and a decrease in CO₂. The
295 possible origin of this high-altitude O₃ depletion will be investigated in Sect. 3.3.1 using individual vertical profiles that exhibit
the same distribution for other flights such as L3 (also T4 or L2 not shown in the study).

O₃ vertical profiles generally increase with altitude, especially in the western flights, and follow a trend opposite to that of CH₄
mixing ratios. Eastern flights present an enhancement of +10 ppb to +20 ppb compared to Mauna Loa and Barrow mixing
ratios respectively at 35 ppb and 30 ppb for the same altitude range, while western mixing ratios agree with the value from
300 Barrow but above the one from Mauna Loa. O₃ and CH₄ measurements are above the corresponding background values and
therefore reflect regional variability of transport that need deeper investigation.

For CO₂, our measurements are comparable to the Mauna Loa monthly mean (411.52 ppm) in the free tropospheric altitude
range of the site (2000-3000 m). Mean CO₂ measured during the western flights in the lowest 1000 m (397-403 ppm) are
consistently lower than the Mace Head monthly mean (406 ppm). On the opposite the eastern flights mean CO₂ below 1000
305 m is relatively similar to the Mace Head mean. The four highest mean CO₂ mixing ratios close to the ground are collected
during eastern profiles (Fig. 5d). These are the three loops of Bering Strait and the transit T6 landing at Yakutsk. For flight T6,
half of the low altitude values were taken in the vicinity of the city of Yakutsk and could be subject to local pollution. CH₄ and
CO as well present high mixing ratios at low altitudes for T6 with respective mixing ratios of 1972 ppb and 103 ppb, and for
T7 with respective mixing ratios of 2045 ppb and 107 ppb. The loops L4.1, L4.2 and L4.3 in remote marine environments will
310 be investigated in Sect. 3.2.2. Flights L4.3 and T5 present a lower CO₂ layer at higher altitude (respectively 6500 m and 5500
m) already noted previously.

These observations show that the atmosphere over Siberia is affected by a complex pattern of influences from local emissions
and long-range transport of polluted air masses. It highlights the importance of untangling the different influences on
atmospheric composition (Petäjä et al., 2021) that will be further discussed in the next section.

315 3.3 Individual vertical profiles and regional atmospheric transport

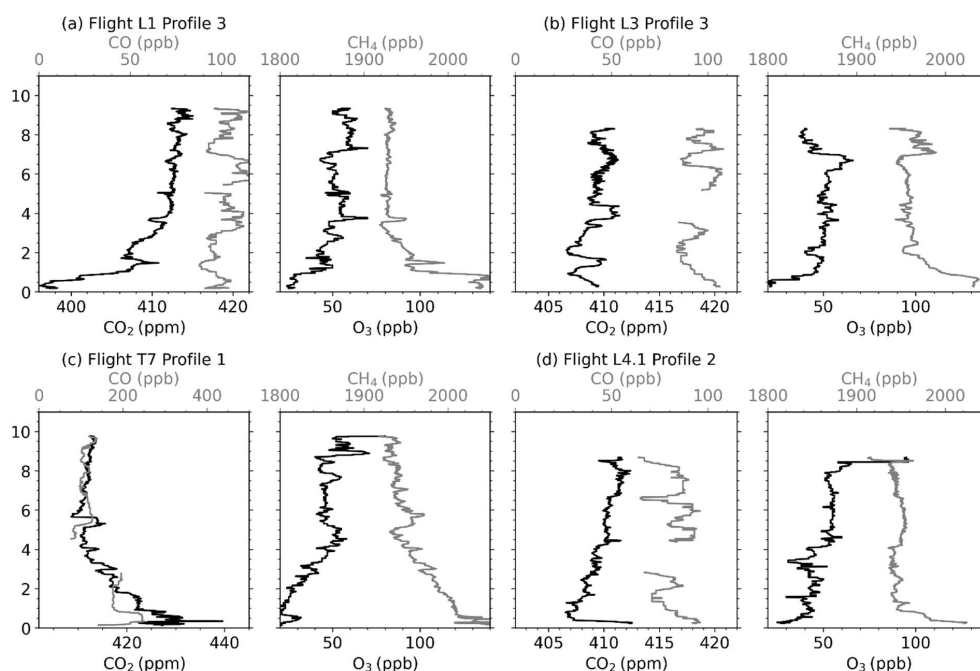
3.3.1 North-Western Russia

Figure 6 displays four selected profiles (either ascent or descent) that are representative of vertical distribution of trace gases
mole fractions encountered during the campaign. Figure 6a is a profile of flight L1 characterized by taiga and wetlands
environments. The flight L1 was highlighted in Sect. 3.1.1. for having the largest CO₂ interquartile range of the whole



320 campaign. Fig. 6b is a profile of flight L3 close to the ESAS. Fig 6c shows a profile of flight T7 crossing the city of Yakutsk
in regions covered by forests of coniferous trees and agricultural lands, and Fig. 6d represents a profile of flight L4.1 located
near the Bering straits in biomes such as Arctic deserts, tundra, and forests tundra.

The vertical profile shown in Fig. 6a presents a large CO₂ depletion of 14 ppm in the lowest 2000 m depth layer, highlighting
the strong drawdown of CO₂ in BL air. Higher altitude air corresponds to free tropospheric air masses that mostly resided over
325 western European countries and United States to finally arrive in Russia from high altitudes (see footprint in Fig. 7a). These
regions are important CO₂ and CH₄ emitters through fossil fuel exploitation and combustion, agriculture and waste
management as documented in the EDGAR inventories (Crippa et al., 2019). This shows that the tropospheric air over the area
of flight L1 is dominated by the outflow of European BL air interplaying with CO₂ uptake in the BL. Both CH₄ and O₃ profiles
present an inversion corresponding to a “chemical” BL around 1000 m (with gradients respectively -90 ppb and +25 ppb).
330 Below 3000 m, CH₄ is anti-correlated with O₃ while the two gases present common features above this altitude, with thin
positively correlated layers at 4000 m and 5000 m.



335 **Figure 6:** Four selected vertical profiles of the campaign. CO₂ and CO are respectively in black and gray on each left plot. O₃ and
CH₄ are respectively in black and gray on each right plot. Please note the different scales for CO₂ and CO.

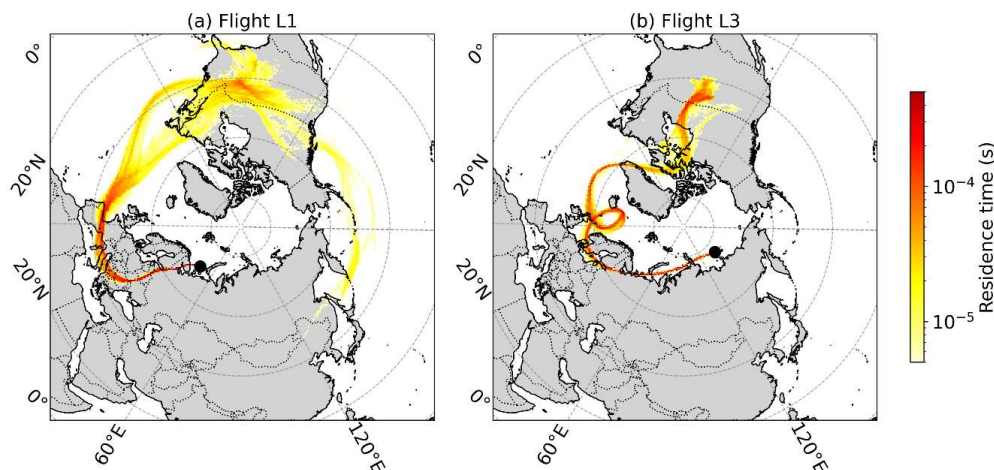


Figure 7: Total column footprints for simulated retro-transport of particles released at 14:53 at an altitude of 9324 m during flight L1 (a) and at 05:01 at an altitude of 5256 m during flight L3 (b). The black dot represents the receptor position.

340

Figure 6b shows the second ascent of L3, in the North of Siberia. Here, CO₂ mole fraction shows less variability than flight L1 profile 3. A slight decrease of -3 ppm of CO₂ and -20 ppb of CO with altitude can be observed under 1000 m, possibly indicating the influence of emissions by local combustion, although this ascent does not start at an airport. We can also observe a stratification in the CO₂ and CO profiles with mixing ratio changes in stacked layers whose thickness varies between 500 m and 1500 m. This stratification has already been observed in previous campaigns (Paris et al. 2008) and is due to slow stirring in the troposphere under reduced vertical mixing. This profile is also characterized by significant sources of CH₄ in the BL as it is suggested by the strong enhancement of 100 ppb close to the ground (Fig. 6b). Among potential sources is methane hydrates degradation from the East Siberian Arctic Shelf (Berchet et al., 2016; Thornton et al., 2016; Berchet et al., 2020). The influence of potential sources will be discussed in Sect 3.4. In the same profile, O₃ is anti-correlated with CH₄ above 3000 m, except at the top altitude around 8500 m where O₃ mole fractions unexpectedly decrease closer to the stratosphere. This O₃ depletion mentioned in Sect 3.2. (-24 ppb compared to immediately lower layers) occurs in the air mass whose history is shown in Fig 7b. The backward transport simulation shows an air mass coming from the BL in Northern America and crossing the Atlantic Ocean and Northern Europe. This layer with poor ozone concentration is likely to be an uplift of BL air with the origin of the depletion potentially coming from another location further upstream. The O₃ mole fraction at top altitude varies from 37 to 40 ppb which is comparable to local mole fraction at 2000 m (40 to 42 ppb) of the same flight, or flight L1 (41 to 42 ppb just under 2000 m) corresponding to regional BL air.

355



3.3.2 Yakutsk urban area

Another singular event formerly mentioned was a possible pollution enhancement in the area of Yakutsk. The corresponding vertical profile in Fig. 6c shows high CO_2 , CH_4 and CO mixing ratios (respectively 439.60 ppm, 2070 ppb and 251 ppb) as the aircraft took off from Yakutsk. At low altitude, both CO and CH_4 present high correlation with CO_2 (respectively $R^2 = 0.92$ and $R^2 = 0.84$) as shown in Fig. 8a and Fig. 8b while there is no correlation at higher altitude. Such suggests combustion emissions possibly related to fossil fuels exploitation and/or use. This region is indeed characterized by the presence of operating O&G infrastructures and coal mines (Fig. 1). We can also observe the lowest O_3 mole fraction of the campaign at 2 ppb at the ground level of Yakutsk (value too low to be seen on the figure). Having this O_3 near-ground minima over landing air-strips in polluted city plumes of Yakutsk suggests a titration of O_3 by NO .

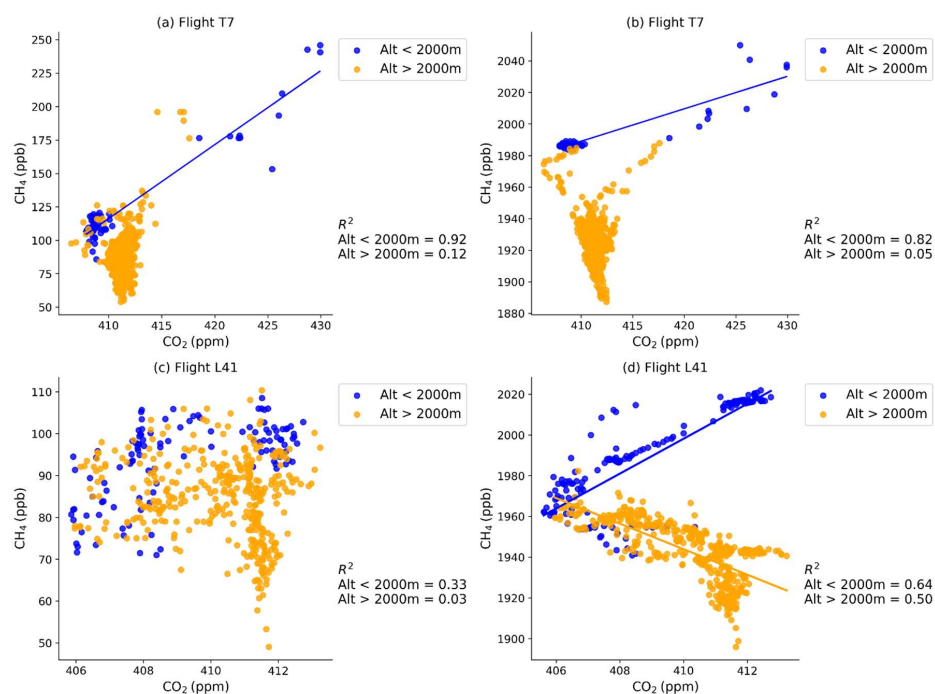


Figure 8: Scatter plots of CO_2 vs CO (a) and CO_2 vs CH_4 (b) for flight T7. Same for flight L4.1 in (c) and (d). Blue dots and respective regression lines are for data acquired under 2000 m. Orange dots and respective regression lines are for data acquired above 2000 m. Correlation coefficient R^2 are a displayed for each set.

370



3.3.3 CO₂ enhancement at low altitude in the East

Flights L4.1, L4.2 and L4.3 over the Bering Strait measured significant CO₂ enhancements at low altitude (Sect. 3.2). Here we focus our analysis on the loop L4.1 as the three flights have similar features. In the vertical profile of the first descent, remote from any airport, a high CO₂ mixing ratio of 412.5 ppm has been observed close to the ground (200m), against 407 ppm at 500 m altitude (Fig. 6d). The CH₄ mixing ratio also decreases from 2025 ppb to 1980 ppb between 200 m and 500 m altitude. On the other hand, CO presents only a small, opposite gradient of about -10 ppb across the same altitude range.

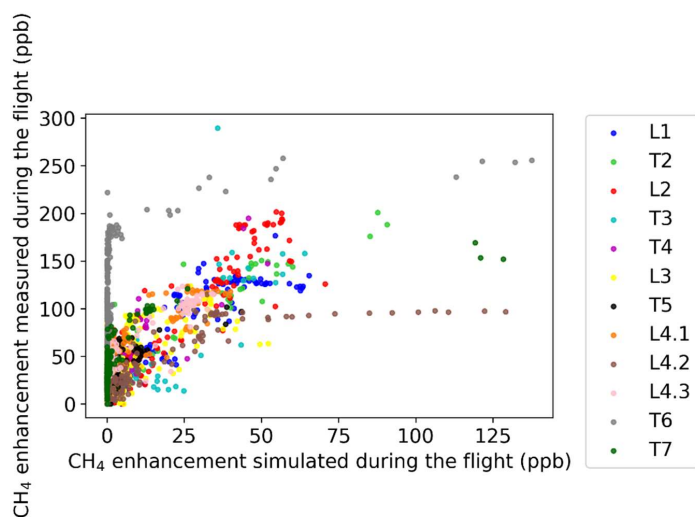
Figure 8c shows a scatter plot of CO against CO₂ for the whole flight L4.1 (including all six profiles). The correlation coefficient under 2000 m is low ($R^2 = 0.33$) suggesting that the CO₂ enhancement may not be strongly driven by emissions from local combustion processes. Fig. 8d presents good correlation between CH₄ and CO₂, both at low and high altitude (respective $R^2 = 0.64$ and $R^2 = 0.50$). The regression slope is 8.5 ppb CH₄ / ppm CO₂. Non-combustion sources emitting both CO₂ and CH₄ leading to such a signature could include one or several fossil fuel exploitation areas co-emitting the two species. According to the Global Fossil Infrastructure Tracker map from Global Monitor Energy, no operating O&G pipelines or terminal is reported in the East Siberian region, and the closest one being Kenai Alaska liquid natural gas terminal (Fig. 1). Still according to Global Energy Monitor, only Amaam North Coal Mine is active in East Siberian region (Fig. 1) but there are other coal mine activities reported in Russian Far East (Petäjä et al., 2021).

Multiple regional and diffuse sources may be at play in explaining the enhancement observed. Another possibility is an emission from marine CH₄ sources. The absence of sea ice at the time of the campaign in the involved area (Fig. B1) (Fetterer et al., 2017) is enabling air-sea exchange, notably for CH₄.

3.4 Untangling the different methane sources with a Lagrangian model

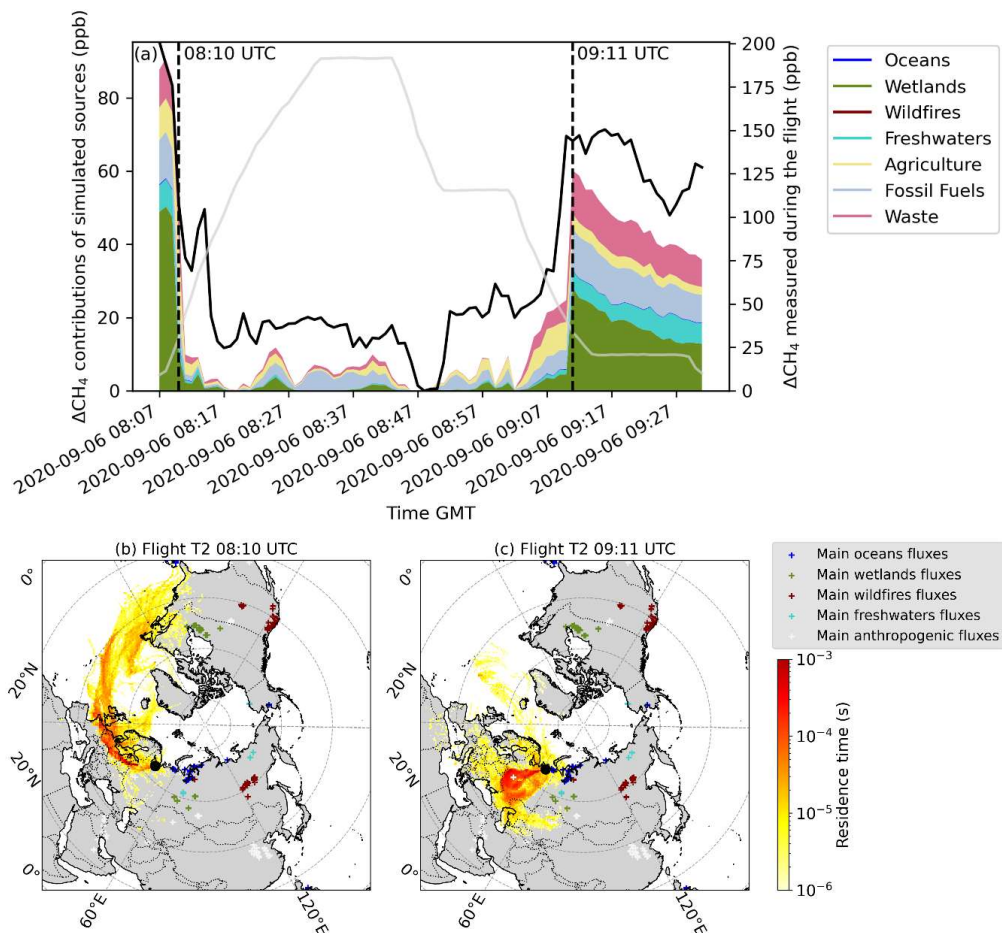
3.4.1 Contributions to measured CH₄ depending on the geographical by source type and location

This section aims at identifying the main emissions influencing the CH₄ concentrations through case studies of selected flights. Fig. 9 shows a scatter plot of measured and simulated CH₄ enhancements for each flight (enhancement being defined here as the measured mixing ratio minus the lowest mixing ratio of the flight). Correlation coefficient R^2 range between 0.26 (for flight T6) and 0.87 (for flight L1), with associated p-values that are inferior to 10^{-10} for every flight. For most flights, the agreements between simulations and measurements are satisfactory and enable comparison of simulated source contributions to observed CH₄ enhancements. However, we will show also that there is an underestimate of simulated mole fractions compared to the measurements. For the study, we select one flight in western Siberia: T2 that has a correlation coefficient $R^2 = 0.85$, and one flight in eastern Siberia: L4.1 that has a correlation coefficient $R^2 = 0.67$.



400 **Figure 9: Scatter plots of simulated CH₄ enhancement vs measured CH₄ for each flight of the campaign except T1. Data were aggregated into 1 min bins to produce this figure.**

Figure 10 shows the simulated CH₄ mole fractions aggregating contributions from tagged sources during flight T2. The simulated signal at the receptor position is compared to measured CH₄ enhancement. The CH₄ enhancement variability is reasonably well reproduced by the model (Fig. 10a) but there is a consistent underestimation in total enhancement values. Some simulated contributions are underestimated by a factor 3 to 4. The possible reasons of this underestimate will be discussed later in Sect. 3.4.2. However, the ability of the model to reproduce the peaks and trough of CH₄ during the entire campaign allows some confidence in the comparative tagged tracer analysis intended here.



410 **Figure 10:** (a) Simulated CH_4 enhancement (coloured stacked plot) and measured CH_4 (black line) for flight T2. Note the different Y-axes. Altitude is shown in grey. The two vertical dotted lines indicate the measurements represented in the following footprints. (b) 10 d potential emission sensitivity (PES) for particles released at 08:17 UTC. (c) Same as (b) at 09:11 UTC. The colored “+” symbols represent the fluxes with biggest intensities derived from each inventory. The black dot represents the receptor position.

415 Figure 10b and c show PES for two selected positions representative for the flight. The footprint in Fig. 10b corresponds to the beginning of the ascent after leaving the airport (first dotted line at 08:10 UTC in panel a). At this position, an enhancement of 50 ppb was simulated. This enhancement is simulated to originate from a dominant anthropogenic contribution distributed



between fossil fuel exploitation, agriculture and waste management for a total of 36 ppb (the following highest contribution being wetlands with 10 ppb of contribution). The footprint Fig. 10b shows that the air mass has mostly resided over Western
420 Russia, Central Europe, the Atlantic and, to a lesser extent USA (although this corresponds to an air mass age close to the limit of particle tracking of 10 days). This is consistent with the dominance of agricultural CH₄ fluxes in anthropogenic fluxes in Europe and the USA (appendix Fig. A1b) while agriculture is much less significant in the Russian emission inventories (Crippa et al., 2019). This documents long-range transport of free tropospheric air masses with relatively high CH₄ (comparable to values encountered in the BL) in western Siberia.

425 The footprint on Fig. 10c, close to the Arctic Ocean at lower altitude (second dotted line at 09:11 UTC in panel a), corresponds to mixed enhancements of 28 ppb by wetlands and 27 ppb by human activities. The PES is concentrated on western Russia, with a major sensitivity to anthropogenic flux at the core representing the city of Moscow (white-filled “plus” sign on Fig. 10c). The simulated enhancements are driven by with the CH₄ fluxes from fossil fuels exploitation and use (appendix Fig. A1a) in western Russia, and from wetlands fluxes in Western Siberia (appendix Fig. A1c), especially in the Vasyugan swamp.

430 At the end of the flight, when getting closer to Naryan Mar, Fig. 10a depicts an enhancement of 7 ppb associated with freshwater sources that is represented by the constant light blue area between 09:11 UTC and the last data at 09:31 UTC. A large number of lakes are present around Naryan Mar and its surroundings (Fig. C1), supporting the importance of freshwater contribution in the atmospheric CH₄ burden. Also, it is likely that a part of the simulated enhancements due to wetlands may be associated to freshwaters CH₄ emissions because there may be some overlap in inventories regarding small lakes and
435 wetlands sources, especially in complex regions with presence of many wetlands, lakes or rivers like in Naryan Mar outskirts. Focusing now on Eastern Siberia, Fig. 11 illustrates the simulated and measured CH₄ enhancements, and two PES footprints associated with two specific positions of the flight. Overall, measured and simulated enhancements are lower than for the Western Siberian flight previously discussed. The first case (00:25 UTC during flight L4.1, first dotted line) is a very thin plume of elevated CH₄ in the lower free troposphere. It has a simulated enhancement of 14 ppb dominated by contributions
440 due to fossil fuel exploitation (7 ppb), agriculture (4 ppb) and waste management (3 ppb). The PES footprint in Fig. 11b shows that the air masses have partially resided over north-east China, very close to fossil fuels exploitation sources (see the white “+” sign on Fig. 11b) and where important CH₄ fluxes from agriculture are present (Fig. A1). Several fossil-fuel extraction infrastructures are located in this region (Global Energy Monitor, 2022). A large part of the air masses has also resided over East China Sea and Bering Strait where there are CH₄ fluxes due to offshore fossil fuel according to EDGAR inventories
445 (appendix Fig. A1) explaining the domination of fossil fuel exploitation contribution in the selected peak.

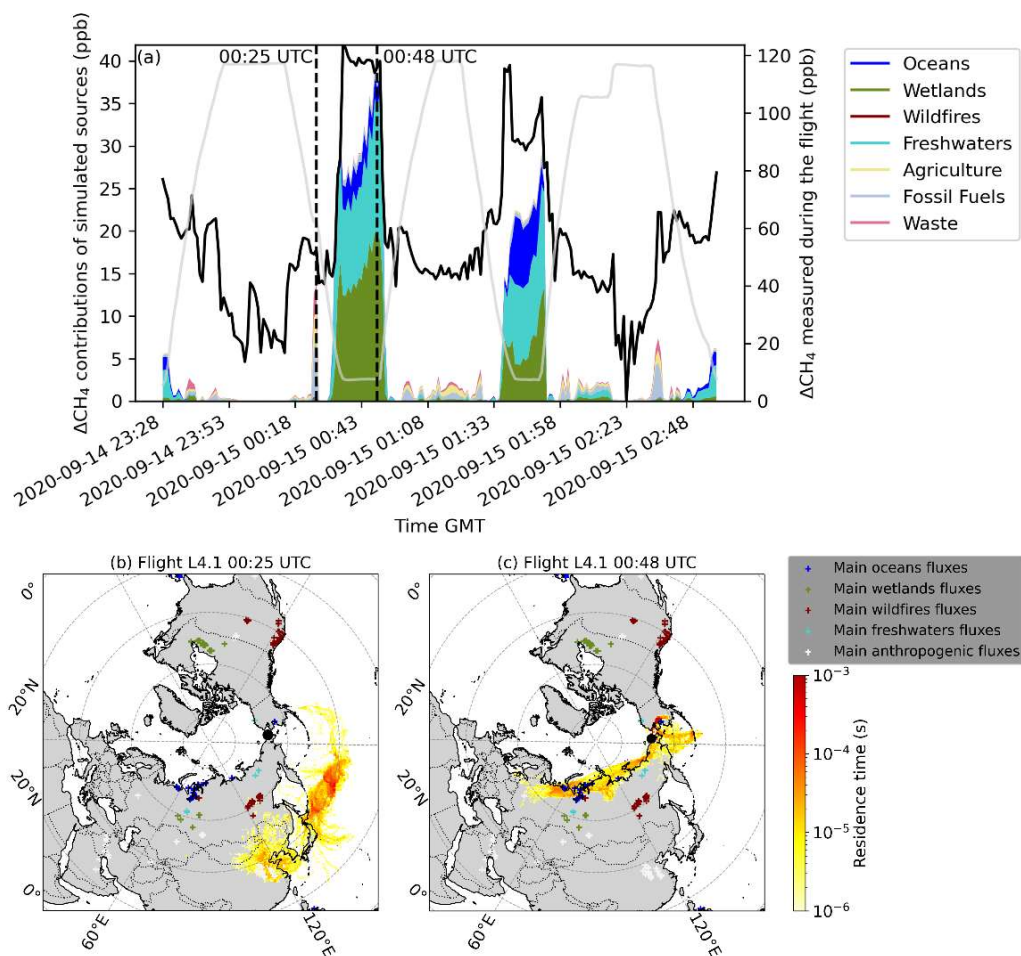


Figure 11: (a) Simulated CH_4 enhancement (coloured stacked plot) and measured CH_4 (black line) for flight L4.2. Note the different Y-axes. Altitude is shown in grey. The two vertical dotted lines indicate the measurements represented in the following footprints. (b) 10 d potential emission sensitivity (PES) for particles released at 22:56 UTC. (c) Same as (b) at 23:42 UTC. The colored “+” symbols represent the fluxes with biggest intensities derived from each inventory. The black dot represents the receptor position.

The second dotted line at 00:48 UTC in Fig. 11a is associated with simulated CH_4 enhancement of 38ppb close to the BL. The simulation indicates that air masses travelled mostly over the Bering Strait, East Siberian Sea and Laptev Sea (Fig. 11c). The



enhancement is dominated (in relative terms) by the freshwater contribution with 15 ppb. Wetlands still play a large role with
455 simulated mixing ratios that can represent 20% to 50% of the peaks at low altitude for this flight. Methane from the Arctic
Ocean significantly appears in the simulated low-altitude enhancement but is lower than the other natural sources, with a
maximum at 8 ppb in the same flight (Fig. 11a).

Over these two flights, we can observe that the peak to peak amplitude of simulated mixing ratios is larger than the amplitude
of measured mixing ratios (e.g. looking at the decrease just after the first peak of Fig. 10a), indicating that some contributions
460 are likely missing in our model. Some simulations though have smaller occurrences of underestimations of observed peaks,
such as flight T3. Wildfires have influenced previous campaigns during specific episodes, especially close to the sources, as
reported in Paris et al. (2008) and in Antokhin et al. (2018). Here we notice the absence of simulated wildfires contribution
throughout the campaign.

The contributions of the oceanic sources are not dominant in the simulation over any freshwater source in this study. Here,
465 freshwaters appear as a dominant term in the CH₄ emitter influencing variability over Northern Siberia. Given the modelling
uncertainties, it is challenging to attribute missing simulated CH₄ to a minor source term. Hence, comparing our simulated
and measured CH₄ time series do not provide sufficient confidence for assuming that the Weber et al. (2019) marine inventory
is underestimated. The two PES footprints reveal a local CH₄ production in this part of Siberia, even in polluted air masses at
high altitude whereas in the West they were resulting from long-range transport. In addition, there might be a sampling bias
470 due to the campaign observation strategy. CH₄ measured from loops flights more often originates from natural sources
compared to in transit flights, which sample BL air essentially in the vicinity of airports. The aircraft flies more frequently at
low altitude and over remote areas during the loop flights.

Overall, our model-data comparison indicated that CH₄ variability in Western Siberia is dominated by a combination of
Western Siberia wetland sources and human activities while eastern Siberia is characterized by strong natural sources such as
475 wetlands, lakes, ponds and, to a smaller extent, oceans.

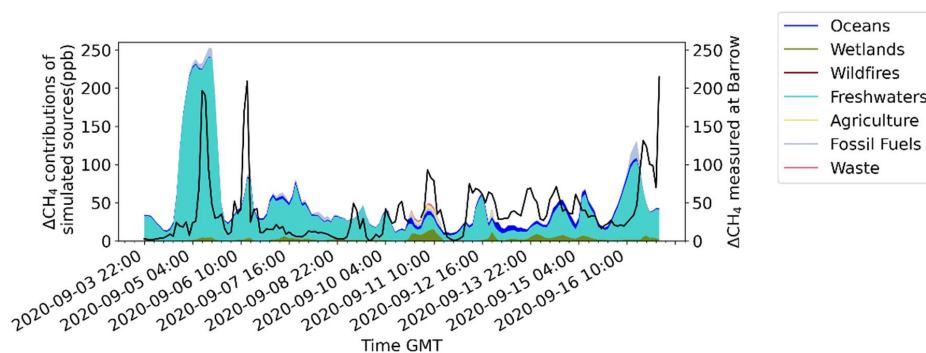
3.4.2 Sources of uncertainties and the underestimation of measurements

Although peaks and trough are well simulated, total CH₄ mole fractions across all flights were consistently underestimated.
While FLEXPART is performing well at high altitudes in representing the signal variability, it has some limitations in
simulating local pollution in the boundary layer. Stohl et al. (1995) reported that the representation of vertical transport leads
480 to greater errors than lateral transport. This might be due either to the low resolution of meteorological data, poor emission
inventory accuracy in Siberia, or a simplification of flux densities under the planetary boundary layer (Stohl et al., 1995). In
addition, the spatial resolution of 1° of the meteorological input data deteriorates the resolution of simulations under the
planetary boundary layer.

Vertical transport across the boundary layer may have a significant role in the model underestimation given the trajectory of
485 our aircraft campaign with large changes in altitude. Figure 12 shows the simulated CH₄ and measured enhancement for the



period of the campaign at Barrow, Alaska (Dlugokencky et al., 2021c), which is obviously not subject to vertical movement of the receptor. Simulated mixing ratios are much less biased compared to the measurements (simulated mean CH₄ being at 52 ppb and Barrow CH₄ mean at 37 ppb). There are some occasional overestimates that might be due to fluxes included in both freshwaters and wetlands inventories. At this time of the year, Barrow is dominated by freshwater emissions from Alaska and Canada whereas anthropogenic emissions are largely absent in the simulation.



495 **Figure 12: Comparison of enhancement of measured CH₄ (black line) and simulated CH₄ (coloured stacked plot) at Barrow station during the whole campaign.**

For some inventories, the specific month of September 2020 was not available in the data. Previous years were used instead. This could lead to some underestimates as we can expect that emissions from some sources may possibly increase with time (e.g. CH₄ from anthropogenic activities) or subject to high temporal variability (CH₄ from natural biogenic sources). Two inventories, EDGAR (anthropogenic fluxes) and ORCHIDEE (fluxes from wetlands), were available for different years. We produced a sensitivity analysis by taking the previous years of these two inventories and producing the simulated mole fractions for the same period. The time of reference is set to the month of September for the last year available of each inventory (2018 for EDGAR and 2017 for ORCHIDEE) and the mole fractions of the two respective years before were also simulated. The simulations exhibit similar patterns, and we extracted the simulated values of the four peaks studied in Sect. 3.4.1. Enhancement's variations induced by changing the year of EDGAR inventories don't exceed 0.4 ppb. Enhancement's variations induced by changing the year of ORDCHIDEE inventories can go up to 5 ppb due to the variability of wetlands emissions. This parameter ultimately appears to have little influence in our simulations that only cover a short period.



Another source of error could be the underestimation of fluxes from poorly-known natural sources such as the marine ones.

510 The estimation of CH₄ emissions by the ocean largely depends on the approach as reported in Weber et al. (2019). However, values vary significantly among the few available studies. For example, methane emissions in East Siberian Arctic Shelf are still uncertain and are estimated to range between 8 and 17 Tg CH₄ yr⁻¹ (Berchet et al., 2016) by oceanographic approach, while an atmospheric inverse estimation provides a flux estimate not higher than 4.5 Tg CH₄ yr⁻¹ (Berchet et al., 2016). As discussed previously, they are influencing CH₄ variability but do not appear to be a dominant term in any part of our flights.

515 Freshwater estimations are also subject to significant variability as it is difficult to be exhaustive in the distribution of the sources and there are fundamentals gaps in the lakes model (Matthews et al., 2020). The “snapshot” effect of methane flux measurements in field campaigns may also leads to underestimates (Wik et al., 2016) or biases. Further works may focus on performing simulations with other inventories such as the one used in Matthews et al. (2020) for high-latitude lakes or the submarine seep estimates from Etiope et al. (2019). On the other hand, it is reported in Matthews et al. (2020) that small

520 wetlands are often interwoven with lakes causing difficulties to distinguish them which leads to overestimates. ORCHIDEE also may overestimate CH₄ net primary production by wetlands due to a lack of wetland specific plant functional types representation (Ringeval et al., 2012; Wania et al., 2013). It could be relevant to test other flux estimated on wetlands and quantify the associated variation to check possible overestimates. The present study only captures a precise moment of the atmospheric condition in Siberia, giving an overview of main phenomena at the end of the summer in the year 2020. Therefore,

525 observations should be completed with medium-term and long-term studies, and the aircraft data could be used as validation data for inverse modelling studies.

4 Conclusion

We have investigated the latest data of September 2020 aircraft campaign over the Russia’s Arctic, including Siberia. It comprised 47 vertical profiles split in 13 flights across all of Siberia giving opportunities to observe CO₂ and CH₄ emissions

530 and transport in different locations of an imperfectly known region that has a serious impact in global carbon budget. In-situ measurements of CO and O₃ have also been performed and are used as complementary tracers in this work.

CO₂ mixing ratios (median value of the campaign at 410.83±3.29 ppm) were slightly lower than Mauna Loa average (411.52 ppm) due to the passage of air masses above CO₂ sinks, and CH₄ mixing ratio (median value of the campaign at 1939±45 ppb) were higher (Mauna Loa average at 1888 ppb), indicating an accumulation of methane from different sources. Western Siberia

535 exhibits steep mole fraction gradients in CO₂ explained by the presence of effective sinks close to the ground (dense vegetation with taiga) while higher altitudes are characterized by the long-range transport of air masses polluted by anthropogenic activities. Eastern Siberia is subject to local pollution and CH₄ emissions from natural sources with less atmospheric transport. Individual vertical profiles also revealed more unique patterns such as the stratification of CO₂ and CO mixing ratios with altitude, the O₃ depletion at top altitude in air masses that crossed Norwegian Sea, and the excess of CO₂ in Bering Strait

540 region. As we wanted to determine if ocean fluxes (and hydrate gas) had a significant role in methane emissions, we simulated



the CH₄ enhancement by different types of sources presents in Siberia. It appeared that emissions are dominated by wetlands, fossil fuel exploitation and agriculture in the West, and by freshwaters and wetlands in the East. Aquatic sources may be underestimated but our measurements are not sufficient to confront existing inventories due to limitations in the numerical models and observational strategy. However, our data suggests that poorly estimated aquatic emissions at regional scale in Arctic Siberia deserve further research and more measurements. With this insight on the main methane sources in northern Russia at the end of summer, we advocate for further research on aquatic CH₄ sources in Siberia to better predict potential positive feedbacks between regional and global warming.

Data availability. In flight measurement data is currently available from the authors upon request (at jean-daniel.paris@lsce.ipsl.fr). Data will be available online with access through: <https://yak.aeris-data.fr/>.

Author contributions. CN performed data processing and simulations, and analysed the data. JDP designed the study. CN and JDP wrote the first version of the manuscript. AB, SW and MS helped to perform simulations. BB, MA, and SB designed, organised and together with DD, AF, and AK performed the aircraft campaign and did the trace gas measurements. All contributed to the manuscript.

Competing interests. None

Acknowledgements. The aircraft campaign was realised by V.E. Zuev Institute of Atmospheric Optics SB RAS under the financial support of Ministry of Science and Higher Education of the Russian Federation (Agreement No. 075-15-2021-934). Data exchange and collaboration was done in the frame of the YAK-AEROSIB MoU. We thank the European Centre for Medium Range Weather Forecasts (ECMWF) for the provision of ERA-Interim reanalysis data, the FLEXPART development team for the provision of the FLEXPART 9.2 model version. We thank Joel Thanwerdas, and Thibaud Thonat for adapting the inventories used in the study. The MEMENTO database is administered by the Kiel Data Management Team at GEOMAR Helmholtz Centre for Ocean Research and supported by the German BMBF project SOPRAN (Surface Ocean Processes in the Anthropocene, <http://sopran.pangaea.de>). The database is accessible through the MEMENTO webpage: <https://memento.geomar.de>.

References

Anokhin G. G., Antokhin P. N., Arshinov M. Yu., Barsuk V. E., Belan B. D., Belan S. B., Davydov D. K., Ivlev G. A., Kozlov A. V., Kozlov V. S., Morozov M. V., Panchenko M. V., Penner I. E., Pestunov D. A., Sikov G. P., Simonenkov D. V., Sinityn



- D. S., Tolmachev G. N., Filipov D. V., Fofonov A. V., Chernov D. G., Shamanaev V. S. and Shmargunov V. P.: OPTIK Tu-134 aircraft laboratory, *Optika Atmosfery i Okeana*, V. 24. No. 09., 805-816, 2011 [in Russian].
- Antokhin, P. N., Arshinova, V. G., Arshinov, M. Y., Belan, B. D., Belan, S. B., Davydov, D. K., Ivlev, G. A., Fofonov, A. V.,
575 Kozlov, A. V., Paris, J. D., Nédélec, P., Rasskazchikova, T. M., Savkin, D. E., Simonenkov, D. V., Sklyadneva, T. K., and Tolmachev, G. N.: Distribution of Trace Gases and Aerosols in the Troposphere Over Siberia During Wildfires of Summer 2012, *J. Geophys. Res-atmos.*, 123, 2285–2297, <https://doi.org/10.1002/2017JD026825>, 2018.
- Bartalev, S. A., Belward, A. S., Erchov, D. V., and Isaev, A. S.: A new SPOT4-VEGETATION derived land cover map of
580 Northern Eurasia, *Int. J. of Remote. Sens.*, 24, 1977–1982, <https://doi.org/10.1080/0143116031000066297>, 2003.
- Belan, B. D., Ancellet, G., Andreeva, I. S., Antokhin, P. N., Arshinova, V. G., Arshinov, M. Y., Balin, Y. S., Barsuk, V. E., Belan, S. B., Chernov, D. G., Davydov, D. K., Fofonov, A. V., Ivlev, G. A., Kotelnikov, S. N., Kozlov, A. S., Kozlov, A. V., Law, K., Mikhal'chishin, A. V., Moseikin, I. A., Nasonov, S. V., Nédélec, P., Okhlopko, O. V., Ol'kin, S. E., Panchenko,
585 M. V., Paris, J.-D., Penner, I. E., Ptashnik, I. V., Rasskazchikova, T. M., Reznikova, I. K., Romanovskii, O. A., Safatov, A. S., Savkin, D. E., Simonenkov, D. V., Sklyadneva, T. K., Tolmachev, G. N., Yakovlev, S. V., and Zenkova, P. N.: Integrated airborne investigation of the air composition over the Russian sector of the Arctic, *Atmos. Meas. Tech.*, 15, 3941–3967, <https://doi.org/10.5194/amt-15-3941-2022>, 2022.
- 590 Belikov, D., Arshinov, M., Belan, B., Davydov, D., Fofonov, A., Sasakawa, M., and Machida, T.: Analysis of the diurnal, weekly, and seasonal cycles and annual trends in atmospheric CO₂ and CH₄ at tower network in Siberia from 2005 to 2016, *Atmosphere-basel.*, 10, <https://doi.org/10.3390/atmos10110689>, 2019.
- Berchet, A., Paris, J. D., Ancellet, G., Law, K. S., Stohl, A., Nédélec, P., Arshinov, M. Y., Belan, B. D., and Ciais, P.:
595 Tropospheric ozone over Siberia in spring 2010: Remote influences and stratospheric intrusion, *Tellus. B.*, 65, 1–14, <https://doi.org/10.3402/tellusb.v65i0.19688>, 2013.
- Berchet, A., Pison, I., Chevallier, F., Paris, J.-D., Bousquet, P., Bonne, J.-L., Arshinov, M. Y., Belan, B. D., Cressot, C., Davydov, D. K., Dlugokencky, E. J., Fofonov, A. V., Galanin, A., Lavrič, J., Machida, T., Parker, R., Sasakawa, M., Spahni,
600 R., Stocker, B. D., and Winderlich, J.: Natural and anthropogenic methane fluxes in Eurasia: a mesoscale quantification by generalized atmospheric inversion, *Biogeosciences*, 12, 5393–5414, <https://doi.org/10.5194/bg-12-5393-2015>, 2015.
- Berchet, A., Bousquet, P., Pison, I., Locatelli, R., Chevallier, F., Paris, J. D., Dlugokencky, E. J., Laurila, T., Hatakka, J.,



605 Viisanen, Y., Worthy, D. E., Nisbet, E., Fisher, R., France, J., Lowry, D., Ivakhov, V., and Hermansen, O.: Atmospheric
constraints on the methane emissions from the East Siberian Shelf, *Atmos. Chem. Phys.*, 16, 4147–4157,
<https://doi.org/10.5194/acp-16-4147-2016>, 2016.

610 Berchet, A., Pison, I., M. Crill, P., Thornton, B., Bousquet, P., Thonat, T., Hocking, T., Thanwerdas, J., Paris, J. D., and
Saunois, M.: Using ship-borne observations of methane isotopic ratio in the Arctic Ocean to understand methane sources in
the Arctic, *Atmos. Chem. Phys.*, 20, 3987–3998, <https://doi.org/10.5194/acp-20-3987-2020>, 2020.

615 Ciais, P., Sabine, C., Govindasamy, B., Bopp, L., Brovkin, V., Canadell, J., Chhabra, A., DeFries, R., Galloway, J., Heimann,
M., Jones, C., Le Quéré, C., Myneni, R., Piao, S., and Thornton, P.: Chapter 6: Carbon and Other Biogeochemical Cycles, in:
Climate Change 2013 The Physical Science Basis, edited by: Stocker, T., Qin, D., and Plattner, G.-K., Cambridge University
Press, Cambridge, 2013.

620 Crippa, M., Oreggioni, G., Guizzardi, D., Muntean, M., Schaaf, E., Lo Vullo, E., Solazzo, E., Monforti-Ferrario, F., Olivier,
J., and Vignati, E.: Fossil CO₂ and GHG emissions of all world countries, Publications Office of the European Union,
Luxembourg, <https://doi.org/doi:10.2760/687800>, 2019.

625 Dlugokencky, E., Mund, J., Crotwell, A., Crotwell, M., and Thoning, K.: Atmospheric Carbon Dioxide Dry Air Mole Fractions,
NOAA GML Carbon Cycle Cooperative Global Air Sampling Network [data set],
<https://doi.org/10.15138/wkgj-f215>, 2021a.

630 Dlugokencky, E., Mund, J., Crotwell, A., Crotwell, M., and Thoning, K.: Atmospheric Methane Dry Air Mole Fractions,
NOAA GML Carbon Cycle Cooperative Global Air Sampling Network [data set],
<https://doi.org/10.15138/wkgj-f215>, 2021b.

630 Dlugokencky, E., Mund, J., Crotwell, A., Crotwell, M., and Thoning, K.: Atmospheric methane from quasi-continuous
measurements at Barrow, Alaska and Mauna Loa, Hawaii, 1986-2020, Version: 2021-03 [data set],
<https://doi.org/10.15138/ve0c-be70>, 2021c.

Elder, C. D., Thompson, D. R., Thorpe, A. K., Hanke, P., Walter Anthony, K. M., and Miller, C. E.: Airborne Mapping Reveals
Emergent Power Law of Arctic Methane Emissions, *Geophys. Res. Lett.*, 47, <https://doi.org/10.1029/2019GL085707>, 2020.



635

Etiope, G., Ciotoli, G., Schwietzke, S., and Schoell, M.: Gridded maps of geological methane emissions and their isotopic signature, *Earth. Syst. Sci. Data.*, 11, 1–22, <https://doi.org/10.5194/essd-11-1-2019>, 2019.

640 Etminan, M., Myhre, G., Highwood, E. J., and Shine, K. P.: Radiative forcing of carbon dioxide, methane, and nitrous oxide: A significant revision of the methane radiative forcing, *Geophys. Res. Lett.*, 43, <https://doi.org/10.1002/2016GL071930>, 2016.

Fetterer, F., Knowles, K., Meier, W. N., Savoie, M., and Windnagel, A. K.: Sea Ice Index, Version 3. [Sea Ice Extent], NSIDC: National Snow and Ice Data Center [data set], Sep 2020, <https://doi.org/https://doi.org/10.7265/N5K072F8>, 2017.

645 Fleming, Z. L., Monks, P. S., and Manning, A. J.: Review: Untangling the influence of air-mass history in interpreting observed atmospheric composition, *Atmos. Res.*, 104–105, 1–39, <https://doi.org/10.1016/j.atmosres.2011.09.009>, 2012.

Friedlingstein, P., O’Sullivan, M., Jones, M. W., Andrew, R. M., Hauck, J., Olsen, A., Peters, G. P., Peters, W., Pongratz, J., Sitch, S., Le Quéré, C., Canadell, J. G., Ciais, P., Jackson, R. B., Alin, S., Aragão, L. E., Armeth, A., Arora, V., Bates, N. R., 650 Becker, M., Benoit-Cattin, A., Bittig, H. C., Bopp, L., Bultan, S., Chandra, N., Chevallier, F., Chini, L. P., Evans, W., Florentie, L., Forster, P. M., Gasser, T., Gehlen, M., Gilfillan, D., Gkritzalis, T., Gregor, L., Gruber, N., Harris, I., Hartung, K., Haverd, V., Houghton, R. A., Ilyina, T., Jain, A. K., Joetzjer, E., Kadono, K., Kato, E., Kitidis, V., Korsbakken, J. I., Landschützer, P., Lefèvre, N., Lenton, A., Lienert, S., Liu, Z., Lombardozi, D., Marland, G., Metzl, N., Munro, D. R., Nabel, J. E., Nakaoka, S. I., Niwa, Y., O’Brien, K., Ono, T., Palmer, P. I., Pierrot, D., Poulter, B., Resplandy, L., Robertson, E., Rödenbeck, C., 655 Schwinger, J., Séférian, R., Skjelvan, I., Smith, A. J., Sutton, A. J., Tanhua, T., Tans, P. P., Tian, H., Tilbrook, B., Van Der Werf, G., Vuichard, N., Walker, A. P., Wanninkhof, R., Watson, A. J., Willis, D., Wiltshire, A. J., Yuan, W., Yue, X., and Zaehle, S.: Global Carbon Budget 2020, *Earth. Syst. Sci. Data.*, 12, 3269–3340, <https://doi.org/10.5194/essd-12-3269-2020>, 2020.

660 Fujita, R., Morimoto, S., Maksyutov, S., Kim, H.-S., Arshinov, M., Brailsford, G., Aoki, S. and Nakazawa, T.: Global and Regional CH₄ Emissions for 1995–2013 Derived From Atmospheric CH₄, δ¹³C-CH₄, and δD-CH₄ Observations and a Chemical Transport Model. *J. Geophys. Res. Atmos.*, 125: e2020JD032903. <https://doi.org/10.1029/2020JD032903>, 2020.

“Global Coal Mine Tracker,” Global Energy Monitor: <https://globalenergymonitor.org/projects/global-coal-mine-tracker/>
665 under the Creative Commons License <https://globalenergymonitor.org/creative-commons-public-license/>, last access: 19
September 2021, 2022.



670 “Global Fossil Infrastructure Tracker,” Global Energy Monitor: <https://globalenergymonitor.org/projects/global-fossil-infrastructure-tracker/tracker-map/> under the Creative Commons License <https://globalenergymonitor.org/creative-commons-public-license/>, last access: 19 September 2021, 2022.

Hazan, L., Tarniewicz, J., Ramonet, M., Laurent, O., and Abbaris, A.: Automatic processing of atmospheric CO₂ and CH₄ mole fractions at the ICOS Atmosphere Thematic Centre, *Atmos. Meas. Tech.*, 9, 4719–4736, <https://doi.org/doi:10.5194/amt-9-4719-2016>, 2016.

675

Hersbach, H., Bell, B., Berrisford, P., Biavati, G., Horányi, A., Muñoz Sabater, J., Nicolas, J., Peubey, C., Radu, R., Rozum, I., Schepers, D., Simmons, A., Soci, C., Dee, D., Thépaut, J.-N. (2018): ERA5 hourly data on single levels from 1979 to present, Copernicus Climate Change Service (C3S) Climate Data Store (CDS) [data set]. (Accessed on 04-10-2021), [10.24381/cds.adbb2d47](https://cds.clm.copernicus.org/cds.adbb2d47), 2018.

680

Kirschke, S., Bousquet, P., Ciais, P., Saunoy, M., Canadell, J. G., Dlugokencky, E. J., Bergamaschi, P., Bergmann, D., Blake, D. R., Bruhwiler, L., Cameron-Smith, P., Castaldi, S., Chevallier, F., Feng, L., Fraser, A., Heimann, M., Hodson, E. L., Houweling, S., Josse, B., Fraser, P. J., Krummel, P. B., Lamarque, J. F., Langenfelds, R. L., Le Quéré, C., Naik, V., O’Doherty, S., Palmer, P. I., Pison, I., Plummer, D., Poulter, B., Prinn, R. G., Rigby, M., Ringeval, B., Santini, M., Schmidt, M., Shindell, D. T., Simpson, I. J., Spahni, R., Steele, L. P., Strode, S. A., Sudo, K., Szopa, S., Van Der Werf, G. R., Voulgarakis, A., Van Weele, M., Weiss, R. F., Williams, J. E., and Zeng, G.: Three decades of global methane sources and sinks, *Nat. Geosci.*, 6, 813–823, <https://doi.org/10.1038/ngeo1955>, 2013.

Kock, A. and Bange, H.: Counting the Ocean’s Greenhouse Gas Emissions, *Eos*, 96, <https://doi.org/10.1029/2015EO023665>,
690 2015.

Lan, X., Nisbet, E. G., Dlugokencky, E. J., and Michel, S. E.: What do we know about the global methane budget? Results from four decades of atmospheric CH₄ observations and the way forward, *Philosophical Transactions of the Royal Society A: Mathematical, Physical and Engineering Sciences*, 379, 20200 440, <https://doi.org/10.1098/rsta.2020.0440>, 2021.

695

Lehner, B. and Döll, P.: Development and validation of a global database of lakes, reservoirs and wetlands, *J. Hydrol.*, 296, 1–22,515 <https://doi.org/10.1016/j.jhydrol.2004.03.028>, 2004.

Masson-Delmotte, V., Zhai, P., Pirani, A., Connors, S. L., Péan, C., Berger, S., Caud, N., Chen, Y., Goldfarb, L., Gomis, M. I.,
700 Huang, M., Leitzell, K., Lonnoy, E., Matthews, J. B. R., Maycock, T. K., Waterfield, T., Yelekçi, O., Yu, R., and Zhou, B.



(Eds.): Climate Change 2021: The Physical Science Basis. Contribution of Working Group I to the Sixth Assessment Report of the Intergovernmental Panel on Climate Change, Cambridge University Press, Cambridge, 2021

705 Matthews, E., Johnson, M. S., Genovese, V., Du, J., and Bastviken, D.: Methane emission from high latitude lakes: methane-centric lake classification and satellite-driven annual cycle of emissions, *Sci. Rep.-uk.*, 10, 1–9, <https://doi.org/10.1038/s41598-020-68246-1>, 2020.

710 Melton, J. R., Wania, R., Hodson, E. L., Poulter, B., Ringeval, B., Spahni, R., Bohn, T., Avis, C. A., Beerling, D. J., Chen, G., Eliseev, A. V., Denisov, S. N., Hopcroft, P. O., Lettenmaier, D. P., Riley, W. J., Singarayer, J. S., Subin, Z. M., Tian, H., Zürcher, S., Brovkin, V., van Bodegom, P. M., Kleinen, T., Yu, Z. C., and Kaplan, J. O.: Present state of global wetland extent and wetland methane modelling: conclusions from a model inter-comparison project (WETCHIMP), *Biogeosciences*, 10, 753–788, <https://doi.org/10.5194/bg-10-753-2013>, 2013.

715 Oltmans, S. J. and Levy, H.: Surface ozone measurements from a global network, *Atmos. Environ.*, 28, 9–24, [https://doi.org/10.1016/1352-2310\(94\)90019-1](https://doi.org/10.1016/1352-2310(94)90019-1), 1994.

720 Paris, J. D., Ciais, P., Nédélec, P., Ramonet, M., Belan, B. D., Arshinov, M. Y., Golitsyn, G. S., Granberg, I., Stohl, A., Cayez, G., Athier, G., Boumard, F., and Cousin, J. M.: The YAK-AEROSIB transcontinental aircraft campaigns: New insights on the transport of CO₂, CO and O₃ across Siberia, *Tellus. B.*, 60, 551–568, <https://doi.org/10.1111/j.1600-0889.2008.00369.x>, 2008.

Paris, J.-D., Stohl, A., Nédélec, P., Arshinov, M. Y., Panchenko, M. V., Shmargunov, V. P., Law, K. S., Belan, B. D., and Ciais, P.: Wildfire smoke in the Siberian Arctic in summer: source characterization and plume evolution from airborne measurements, *Atmos. Chem. Phys.*, 9, 9315–9327, <https://doi.org/10.5194/acp-9-9315-2009>, 2009.

725 Paris, J.-D., Ciais, P., Nédélec, P., Stohl, A., Belan, B. D., Arshinov, M. Y., Carouge, C., Golitsyn, G. S., and Granberg, I. G.: New Insights on the Chemical Composition of the Siberian Air Shed From The Yak-Aerosib Aircraft Campaigns, *B. Am. Meteorol. Soc.*, 91, 625–642, <https://doi.org/10.1175/2009BAMS2663.1>, 2010.

730 Parmentier, F. J. W., Christensen, T. R., Rysgaard, S., Bendtsen, J., Glud, R. N., Else, B., van Huissteden, J., Sachs, T., Vonk, J. E., and Sejr, M. K.: A synthesis of the arctic terrestrial and marine carbon cycles under pressure from a dwindling cryosphere, *Ambio.*, 46, 53–69, <https://doi.org/10.1007/s13280-016-0872-8>, 2017.

Petäjä, T., Ganzei, K. S., Lappalainen, H. K., Tabakova, K., Makkonen, R., Räisänen, J., Chalov, S., Kulmala, M.,



- Zilitinkevich, S., Baklanov, P. Y., Shakirov, R. B., Mishina, N. V., Egidarev, E. G., and Kondrat'ev, I. I.: Research agenda for
735 the Russian Far East and utilization of multi-platform comprehensive environmental observations, *Int. J. Digit. Earth.*, 14,
311–337, <https://doi.org/10.1080/17538947.2020.1826589>, 2021.
- Pisso, I., Sollum, E., Grythe, H., Kristiansen, N. I., Cassiani, M., Eckhardt, S., Arnold, D., Morton, D., Thompson, R. L., Groot
Zwaafink, C. D., Evangeliou, N., Sodemann, H., Haimberger, L., Henne, S., Brunner, D., Burkhart, J. F., Fouilloux, A.,
740 Brioude, J., Philipp, A., Seibert, P., and Stohl, A.: The Lagrangian particle dispersion model FLEXPART version 10.4, *Geosci.
Model. Dev.*, 12, 4955–4997, <https://doi.org/10.5194/gmd-12-4955-2019>, 2019.
- Platt, S., Eckhardt, S., Ferré, B., Fisher, R., Hermansen, O., Jansson, P., Lowry, D., Nisbet, E., Pisso, I., Schmidbauer, N.,
Silyakova, A., Stohl, A., Svendby, T., Vadakkepuliambatta, S., Mienert, J., and Lund Myhre, C.: Methane at svalbard and
745 over the european arctic ocean, *Atmos. Chem. Phys.*, 18, 17 207–17 224, <https://doi.org/10.5194/acp-18-17207-2018>, 2018.
- Reeves, C. E., Penkett, S. A., Bauguitte, S., Law, K. S., Evans, M. J., Bandy, B. J., Monks, P. S., Edwards, G. D., Phillips, G.,
Barjat, H., Kent, J., Dewey, K., Schmitgen, S., and Kley, D.: Potential for photochemical ozone formation in the troposphere
over the North Atlantic as derived from aircraft observations during ACSOE, *Journal of Geophysical Research D:
750 Atmospheres*, 107, <https://doi.org/10.1029/2002JD002415>, 2002.
- Ringeval, B., Decharme, B., Piao, S. L., Ciais, P., Papa, F., de Noblet-Ducoudré, N., Prigent, C., Friedlingstein, P., Gouttevin,
I., Koven, C., and Ducharne, A.: Modelling sub-grid wetland in the ORCHIDEE global land surface model: evaluation against
755 river discharges and remotely sensed data, *Geosci. Model. Dev.*, 5, 941–962, <https://doi.org/10.5194/gmd-5-941-2012>, 2012.
- Rosentreter, J. A., Borges, A. V., Deemer, B. R., Holgerson, M. A., Liu, S., Song, C., Melack, J., Raymond, P. A., Duarte, C.
M., Allen, G. H., Olefeldt, D., Poulter, B., Battin, T. I., and Eyre, B. D.: Half of global methane emissions come from highly
variable aquatic ecosystem sources, *Nat. Geosci.*, 14, 225–230, <https://doi.org/10.1038/s41561-021-00715-2>, 2021.
- 760 Ruppel, C.: Permafrost-Associated Gas Hydrate: Is It Really Approximately 1 % of the Global System?, *J. Chem. Eng. Data.*,
60, 429–436, <https://doi.org/10.1021/je500770m>, 2015.
- Saunois, M., Bousquet, P., Poulter, B., Peregon, A., Ciais, P., Canadell, J. G., Dlugokencky, E. J., Etiope, G., Bastviken, D.,
Houweling, S., Janssens-Maenhout, G., Tubiello, F. N., Castaldi, S., Jackson, R. B., Alexe, M., Arora, V. K., Beerling, D. J.,
765 Bergamaschi, P., Blake, D. R., Brailsford, G., Brovkin, V., Bruhwiler, L., Crevoisier, C., Crill, P., Covey, K., Curry, C.,
Frankenberg, C., Gedney, N., Höglund-Isaksson, L., Ishizawa, M., Ito, A., Joos, F., Kim, H.-S., Kleinen, T., Krummel, P.,



- Lamarque, J.-F., Langenfelds, R., Locatelli, R., Machida, T., Maksyutov, S., McDonald, K. C., Marshall, J., Melton, J. R., Morino, I., Naik, V., O'Doherty, S., Parmentier, F.-J. W., Patra, P. K., Peng, C., Peng, S., Peters, G. P., Pison, I., Prigent, C., Prinn, R., Ramonet, M., Riley, W. J., Saito, M., Santini, M., Schroeder, R., Simpson, I. J., Spahni, R., Steele, P., Takizawa, A., Thornton, B. F., Tian, H., Tohjima, Y., Viovy, N., Voulgarakis, A., van Weele, M., van der Werf, G. R., Weiss, R., Wiedinmyer, C., Wilton, D. J., Wiltshire, A., Worthy, D., Wunch, D., Xu, X., Yoshida, Y., Zhang, B., Zhang, Z., and Zhu, Q.: The global methane budget 2000–2012, *Earth. Syst. Sci. Data.*, 8, 697–751, <https://doi.org/10.5194/essd-8-697-2016>, 2016.
- 770
- Saunois, M., Stavert, A. R., Poulter, B., Bousquet, P., Canadell, J. G., Jackson, R. B., Raymond, P. A., Dlugokencky, E. J., Houweling, S., Patra, P. K., Ciais, P., Arora, V. K., Bastviken, D., Bergamaschi, P., Blake, D. R., Brailsford, G., Bruhwiler, L., Carlson, K. M., Carrol, M., Castaldi, S., Chandra, N., Crevoisier, C., Crill, P. M., Covey, K., Curry, C. L., Etiope, G., Frankenberg, C., Gedney, N., Hegglin, M. I., Höglund-Isaksson, L., Hugelius, G., Ishizawa, M., Ito, A., Janssens-Maenhout, G., Jensen, K. M., Joos, F., Kleinen, T., Krummel, P. B., Langenfelds, R. L., Laruelle, G. G., Liu, L., Machida, T., Maksyutov, S., McDonald, K. C., McNorton, J., Miller, P. A., Melton, J. R., Morino, I., Müller, J., Murguía-Flores, F., Naik, V., Niwa, Y., Noce, S., O'Doherty, S., Parker, R. J., Peng, C., Peng, S., Peters, G. P., Prigent, C., Prinn, R., Ramonet, M., Regnier, P., Riley, W. J., Rosentretter, J. A., Segers, A., Simpson, I. J., Shi, H., Smith, S. J., Steele, L. P., Thornton, B. F., Tian, H., Tohjima, Y., Tubiello, F. N., Tsuruta, A., Viovy, N., Voulgarakis, A., Weber, T. S., van Weele, M., van der Werf, G. R., Weiss, R. F., Worthy, D., Wunch, D., Yin, Y., Yoshida, Y., Zhang, W., Zhang, Z., Zhao, Y., Zheng, B., Zhu, Q., Zhu, Q., and Zhuang, Q.: The Global Methane Budget 2000–2017, *Earth. Syst. Sci. Data.*, 12, 1561–1623, <https://doi.org/10.5194/essd-12-1561-2020>, 2020.
- 785
- Sasakawa, M., Shimoyama, K., Machida, T., Tsuda, N., Suto, H., Arshinov, M., Davydov, D., Fofonov, A., Krasnov, O., Saeki, T., Koyama, Y., and Maksyutov, S.: Continuous measurements of methane from a tower network over Siberia, *Tellus B: Chemical and Physical Meteorology*, 62:5, 403–416, DOI: 10.1111/j.1600-0889.2010.00494.x, 2010.
- 790
- Sasakawa, M., Machida, T., Ishijima, K., Arshinov, M., Patra, P. K., Ito, A., Aoki, S., and Petrov, V.: Temporal characteristics of CH₄ vertical profiles observed in the West Siberian Lowland over Surgut from 1993 to 2015 and Novosibirsk from 1997 to 2015. *Journal of Geophysical Research: Atmospheres*, 122, 11,261– 11,273. <https://doi.org/10.1002/2017JD026836>, 2017.
- 795
- Seibert, P. and Frank, A.: Source-receptor matrix calculation with a Lagrangian particle dispersion model in backward mode, *Atmos. Chem. Phys.*, 4, 51–63, <https://doi.org/10.5194/acp-4-51-2004>, 2004.
- Shakhova, N., Semiletov, I., Salyuk, A., Yusupov, V., Kosmach, D., and Gustafsson, O.: Extensive Methane Venting to the



- 800 Atmosphere from Sediments of the East Siberian Arctic Shelf, *Science.*, 327, 1246–1250,
<https://doi.org/10.1126/science.1182221>, 2010.
- 805 Skorokhod, A. I., Berezina, E. V., Moiseenko, K. B., Elansky, N. F., and Belikov, I. B.: Benzene and toluene in the surface air of northern Eurasia from TROICA-12 campaign along the Trans-Siberian Railway, *Atmos. Chem. Phys.*, 17, 5501–5514,
<https://doi.org/10.5194/acp-17-5501-2017>, 2017.
- 810 Stohl, A. and Thomson, D. J.: A Density Correction for Lagrangian Particle Dispersion Models, *Bound-Lay. Meteorol.*, 90,
155–167, <https://doi.org/10.1023/A:1001741110696>, 1999.
- 815 Stohl, A., Wotawa, G., Seibert, P., and Kromp-Kolb, H.: Interpolation Errors in Wind Fields as a Function of Spatial and
Temporal Resolution and Their Impact on Different Types of Kinematic Trajectories, *J. Appl. Meteorol.*, 34, 2149–2165,
[https://doi.org/10.1175/1520-0450\(1995\)034<2149:IEIWFA>2.0.CO;2](https://doi.org/10.1175/1520-0450(1995)034<2149:IEIWFA>2.0.CO;2), 1995.
- 820 Stohl, A., Hittenberger, M., and Wotawa, G.: Validation of the lagrangian particle dispersion model FLEXPART against large-
scale tracer experiment data, *Atmos. Environ.*, 32, 4245–4264, [https://doi.org/10.1016/S13522310\(98\)00184_8](https://doi.org/10.1016/S13522310(98)00184_8), 1998.
- 825 Stohl, A., Forster, C., Frank, A., Seibert, P., and Wotawa, G.: Technical note: The Lagrangian particle dispersion model
FLEXPART version 6.2, *Atmos. Chem. Phys.*, 5, 2461–2474, <https://doi.org/10.5194/acp-5-2461-2005>, 2005.
- 830 Stöckli, R., Vermote, E., Saleous, N., Simmon, R., and Herring, D.: The Blue Marble Next Generation - A true color earth
dataset including seasonal dynamics from MODIS., corresponding author: rstockli@climate.gsfc.nasa.gov.
- Tan, Z., Zhuang, Q., and Walter Anthony, K.: Modeling methane emissions from arctic lakes: Model development and site-
level study, *J. Adv. Model. Earth. Sy.*, 7, 459–483, <https://doi.org/10.1002/2014MS000344>, 2015.
- 825 Thonat, T., Saunois, M., Bousquet, P., Pison, I., Tan, Z., Zhuang, Q., Crill, P. M., Thornton, B. F., Bastviken, D., Dlugokencky,
E. J., Zimov, N., Laurila, T., Hatakka, J., Hermansen, O., and Worthy, D. E. J.: Detectability of Arctic methane sources at six
sites performing continuous atmospheric measurements, *Atmos. Chem. Phys.*, 17, 8371–8394, <https://doi.org/10.5194/acp-17-8371-2017>, 2017
- 830 Thornton, B. F., Geibel, M. C., Crill, P. M., Humborg, C., and Mörth, C. M.: Methane fluxes from the sea to the atmosphere
across the Siberian shelf seas, *Geophys. Res. Lett.*, 43, 5869–5877, <https://doi.org/10.1002/2016GL068977>, 2016.



- Thornton, B. F., Prytherch, J., Andersson, K., Brooks, I. M., Salisbury, D., Tjernström, M., and Crill, P. M.: Shipborne eddy covariance observations of methane fluxes constrain Arctic sea emissions, *Sci. Adv.*, 6, 1–11, 855 <https://doi.org/10.1126/sciadv.aay7934>, 2020.
- Turetsky, M. R., Jones, M., Walter Anthony, K., Olefeldt, D., Schuur, E. A., Koven, C., McGuire, A. D., and Grosse, G.: Permafrost collapse is accelerating carbon release, *Nature.*, 569, 32–24, 2019.
- 840 van der Werf, G. R., Randerson, J. T., Giglio, L., van Leeuwen, T. T., Chen, Y., Rogers, B. M., Mu, M., van Marle, M. J. E., Morton, D. C., Collatz, G. J., Yokelson, R. J., and Kasibhatla, P. S.: Global fire emissions estimates during 1997–2016, *Earth Syst. Sci. Data.*, 9, 697–720, <https://doi.org/10.5194/essd-9-697-2017>, 2017.
- Wania, R., Melton, J. R., Hodson, E. L., Poulter, B., Ringeval, B., Spahni, R., Bohn, T., Avis, C. A., Chen, G., Eliseev, A. V., 845 Hopcroft, P. O., Riley, W. J., Subin, Z. M., Tian, H., Van Bodegom, P. M., Kleinen, T., Yu, Z. C., Singarayer, J. S., Zürcher, S., Lettenmaier, D. P., Beerling, D. J., Denisov, S. N., Prigent, C., Papa, F., and Kaplan, J. O.: Present state of global wetland extent and wetland methane modelling: Methodology of a model inter-comparison project (WETCHIMP), *Geosci. Model. Dev.*, 6, 617–641, <https://doi.org/10.5194/gmd-6-617-2013>, 2013.
- 850 Weber, T., Wiseman, N. A., and Kock, A.: Global ocean methane emissions dominated by shallow coastal waters, *Nat. Commun.*, 10, 1–10, <https://doi.org/10.1038/s41467-019-12541-7>, 2019.
- Wik, M., Thornton, B. F., Bastviken, D., Uhlbäck, J., and Crill, P. M.: Biased sampling of methane release from northern lakes: A problem for extrapolation, *Geophys. Res. Lett.*, 43, 1256–1262, <https://doi.org/10.1002/2015GL066501>, 2016. 855
- World Meteorological Organization (WMO). Greenhouse Gas Bulletin- No.17: The State of Greenhouse Gases in the Atmosphere Based on Global Observations through 2020. 2021.
- YAK-Aerosol Measurements: <https://yak.aeris-data.fr/welcome/measurements/>, last access: 19 September 2021. 860
- Zhang, Z., Fluet-Chouinard, E., Jensen, K., McDonald, K., Hugelius, G., Gumbrecht, T., Carroll, M., Prigent, C., Bartsch, A., and Poulter, B.: Development of the global dataset of Wetland Area and Dynamics for Methane Modeling (WAD2M), *Earth Syst. Sci. Data*, 13, 2001–2023, <https://doi.org/10.5194/essd-13-2001-2021>, 2021



865 **Appendix A: Additional material on inventories**

A1 EDGAR V6.0 Inventories used and sub-categories created

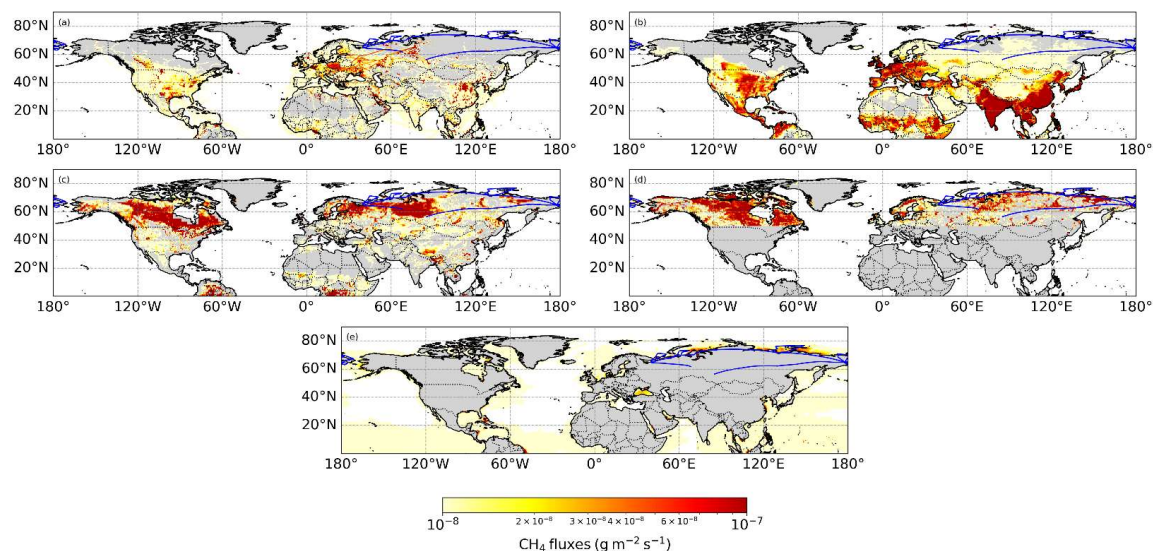
Table A1: The 21 EDGAR V6.0 inventories used for the present study regrouped in three different sub-categories.

Folder name	Name	Our Category
ENE	Power Industry	Fossil fuels exploitation
REF_TRF	Oil refineries and Transformation industry	
IND	Combustion for manufacturing	
CHE	Chemical processes	
IRO	Iron and steel production	
TNR_Aviation_CDS	Aviation climbing & descent	
TNR_Aviation_CRS	Aviation cruise	
TNR_Aviation_LTO	Aviation landing & takeoff	
TRO	Road transportation	
TNR_Other	Railways, pipelines, off-road transport	
TNR_Ship	Shipping	
PRO_coal	Fuel exploitation COAL	
PRO_oil	Fuel exploitation OIL	
PRO_gas	Fuel exploitation GAS	
FFF	Fossil fuel fires	
ENF	Enteric fermentation	Agriculture
MNM	Manure management	
AGS	Agricultural soils	



SWD_LDF	Solid waste landfills	Waste management
SWD_INC	Solid waste incineration	
WWT	Wastewater handling	

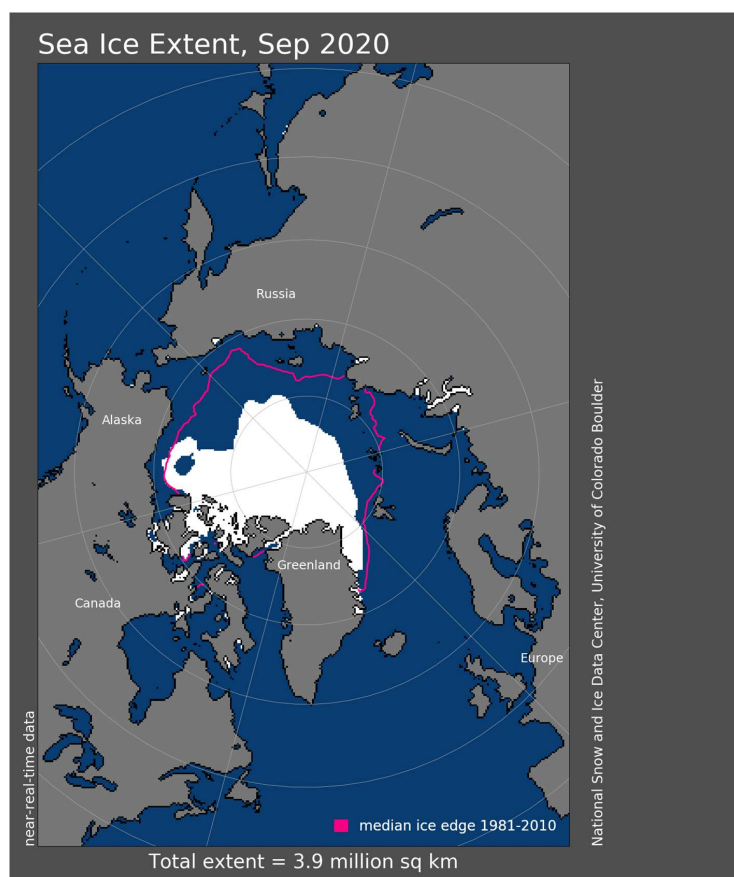
A2 Graphical representation of the main inventories used



870 **Figure A1:** (a) Graphical representation of CH₄ fluxes due to fossil fuel exploitation as reported in appendix Table A1 by EDGAR inventories. The trajectory of the campaign is represented by the blue line. (b) Same as (a) for agriculture by EDGAR. (c) same as (a) for wetlands by ORCHIDEE. (d) same as (a) for freshwaters by blake4me&GLWD. (e) same as (a) for oceans by Weber.



Appendix B: Additional material concerning CO₂ enhancements at low altitude in east Siberia



875 **Figure B1:** Sea ice extent in September 2020. As illustrated, there is no sign of ice in Bering Strait (Fetterer et al., 2017).



Appendix C: Additional material concerning CH₄ freshwater enhancements in Naryan Mar region

880 **C1 Tundra around Naryan Mar**



Figure C1: An aerial picture of the tundra around Naryan Mar revealing the presence of a huge number of lakes in the region. The picture was provided by Boris D. Belan.